

An Efficient Fluorogenic “Turn-on” Dual Chemosensor for Al³⁺ and Zn²⁺ with Distinct Colour Change and Its AIEE Behaviour

7.1. Introduction

Organic luminescent materials that show fluorescence in solid state have been paying attention owing to its potential applications in fluorescence sensors [387], semi conductor lasers [388], optoelectronic devices [389] etc. Luminescent organic aggregates such as amorphous solids, nanocrystals or microcrystals are found to be much more photostable than isolated molecules [390]. On the other hand these aggregates evoke significant interest for their potential applications in sensors, flat panel display and illumination, etc. [391-394] due to their unique photophysical properties and low cost structural design. Most organic luminescent materials exhibits strong emission in their dilute solution, but their emissions disappeared hastily on increasing concentrations in solution or aggregations in solid state because of strong intermolecular π - π stacking interactions and other non-radiative decay pathways. This phenomenon is popularly known as Aggregation Caused Quenching (ACQ) effect [395]. Some anti-ACQ materials were reported by Tang [396] and Park [397] This unique characteristic differentiates them from conventional luminophores and focused on the exploration of their utilities in the development of optical sensors and other potential applications. Their mechanisms of action are usually explained in terms of, restriction of intramolecular rotation (RIR) [398], and vibrations (RIV) [399], intramolecular charge-transfer (ICT) [400] process, intramolecular hydrogen bond [401] etc. Fluorophores showing aggregation induced emission enhancement (AIEE) characteristics have successfully been utilized in organic light emitting diodes (OLEDs) [402], electroluminescent materials [403] photoemitters [404], mechanochromism [405], sensors [406-408] etc.

Development of molecular sensors for selective cation sensing is significant for a host of relevant environmental, biological and diagnostic applications [409-411]. Aluminum is the third most abundant and prevalent element after oxygen and silicon in the earth's crust [412-414]. According to WHO report, the average daily human intake of aluminum is ca. 3–10 mg per day. Tolerable weekly aluminium intake in the human body is estimated to be 7 mg/kg body weight [415]. Excessive exposure of Al³⁺ to the human body leads to lots of diseases such as decrease liver and kidney function, gastrointestinal problems, microcytic hypochromic anemia, memory loss, etc. The toxicity of aluminium causes spoil of the central nervous system and is supposed to be concern in neurodegenerative diseases such as Alzheimer's and Parkinson's [416, 417] and is liable for intoxication in hemodialysis patients

[418]. It is reasonable that increase of free Al^{3+} from soil by human activities is poisonous to growing plants [419]. The general population is uncovered to aluminium from its prevalent use in water treatment, food additive, packaging materials, aluminium based pharmaceuticals, aluminium containers, computers, electrical equipment and many others [415, 420-422]. On the other hand, amongst the cations, zinc also plays a vital role in a plethora of biological processes and has noteworthy implications in healthcare [423-425]. Zinc is the second most abundant transition metal and a necessary element to protect life [426] with 2- 4 g distributed throughout the human body [427]. Various studies reveal that Zn^{2+} has an significant role in biological processes, e.g., cellular metabolism, brain function, and immune function [428, 429]. The permissible nutritional intake of zinc for humans is about 8–11 mg/day [430]. At concentrations higher than the permissible limit, zinc can restrain the uptake of other dietary trace metals such as copper and iron [431]. However, the inconsistency of Zn^{2+} in the human body may cause several neurological disorders, diabetes, Alzheimer's disease etc [432]. Although zinc is a relatively nontoxic, it can be toxic if consumed beyond the permissible limit. For example, significant concentrations of zinc may reduce the soil microbial activity and it is a common contaminant in agricultural and food wastes.

In connection with the sensing of biologically and environmentally relevant ions, fluorescence based tools are considered to have enhanced the capabilities for sensing of specific target analytes [433, 434]. A fluorescent probe produces a detectable fluorescent signal upon interaction with a chemical species [435] and a number of mechanisms like photo induced electron/energy transfer (PET) [436], chelation-enhanced fluorescence (CHEF) [437], fluorescence resonance energy transfer (FRET) [438], metal–ligand charge transfer (MLCT) [439], excited-state intra/intermolecular proton transfer (ESIPT) [440], excimer/excimer formation [441], intramolecular charge transfer (ICT) [442], and C=N isomerisation [443] are being used to explain the chemo sensing processes. Compare to other transition metal ions, selective chemosensors for Al^{3+} are limited due to its poor coordination power and lack of spectroscopic characteristics [444-448]. It has been observed that as a hard acid Al^{3+} prefers hard base containing N and O donor atoms [449]. Consequently, it is highly demanding to develop simply synthesizable fluorescent chemosensors for selective and rapid recognition of Al^{3+} . On the other hand, there has been increasing interest to develop highly selective and sensitive chemosensor for Zn^{2+} among the researchers. Fluorogenic chemosensor is found to be primary choice for Zn^{2+} detection due to its closed shell configuration ($3d_{10}4s_0$) which does not produce spectroscopic or magnetic signals [450,451]. Due to the importance of Al^{3+} and Zn^{2+} , many fluorescent chemosensors for separate

detection of Al^{3+} ions and Zn^{2+} ions have been reported. Yet, most of them contain potential toxic substance in their ingredients, which will pollute the environment and harm human health. Additionally, many chemosensors need complicated syntheses involving harsh reaction conditions and expensive chemicals. More significantly, very few fluorescent chemosensors can selectively detect both Al^{3+} and Zn^{2+} simultaneously [452, 453]. So, it is desirable to develop fluorescent chemosensors with high sensitivity and selectivity for multi-metal ions.

Considering the above fact, we successfully synthesized simple antipyrine based Schiff base 4-[(2-Hydroxy-3-methoxy-benzylidene)-amino]-1,5-dimethyl-2-phenyl-1,2-dihydro-pyrazol-3-one (\mathbf{P}^5) with potential hard N, O donor atoms through a simple one-step synthetic process, where free rotating groups antipyrine and hydroxy benzene moieties are attached to the azo group. Schiff base was found to be poorly fluorescent in good solvent, in part due to isomerization through rotation around the C=N double bond in the excited state [57]. But our synthesized \mathbf{P}^5 as a fluorescent “turn on” chemosensor can recognize selectively both Al^{3+} and Zn^{2+} ion via CHEF process. On the other hand, Aggregated \mathbf{P}^5 exhibits AIEE effect and strong yellow fluorescence is observed under ultraviolet irradiation. Microstructures of \mathbf{P}^5 with various morphologies have been synthesized using SDS as morphology directing agent.

7.2. Experimental section

7.2.1. Materials

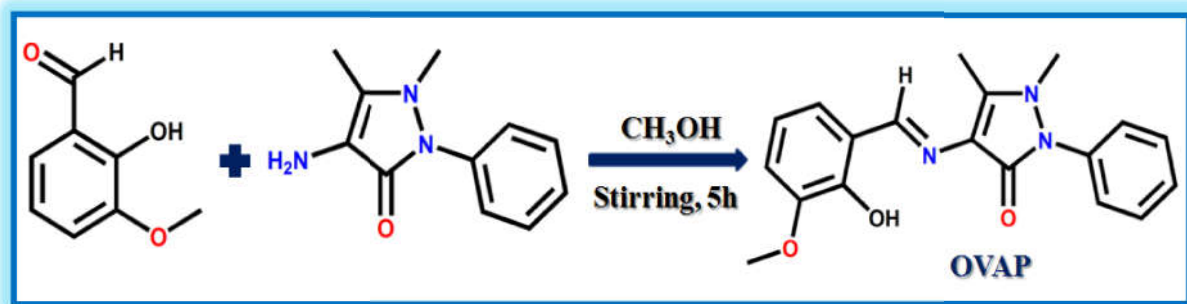
4-aminoantipyrine was purchased from Merck India Ltd. Ortho-Vanillin was purchased from Sigma-Aldrich Chemical Corp. All the solvents used were of analytical grade. Sodium dodecyl sulphate (SDS) was purchased from Merck India Ltd. and was recrystallized from 1:1 ethanol water mixture. Purity of these chemicals was checked spectrophotometrically. Salts (Nitrate and chloride) of all cations (Aldrich and Merck) were of high purity and used without further purification. Triply distilled deionized water was used throughout the experiments.

7.2.2. Synthesis of \mathbf{P}^5 and \mathbf{P}^5 -Microparticles

Ortho-Vanillin (1 equiv) was added to 4-aminoantipyrine (1 equiv) in 50 mL methanol with constant stirring for 5h. The reaction was monitored by thin-layer chromatography. After completion, pale yellow color solid product was filtered, washed thoroughly with methanol, recrystallized and then dried in a desiccators. Yield: 82%. Anal. Calcd for $\text{C}_{19}\text{H}_{19}\text{N}_3\text{O}_3$: C, 67.64%; H, 5.68%; N, 12.46%; Found: C, 67.28%; H, 5.29%; N,

12.23%. FT-IR (KBr), ν , cm^{-1} : 3431 (O – H), 1665 (C = O), 1598 (C = N), 1459, 1411 (C = C), 1296, 1249 (C–O), 1136 (O – H). ^1H NMR (400 MHz, CDCl_3) δ (ppm): 13.92 (H, s (OH)), 9.84 (H, s (–CH=N)), 7.53–6.83 (8H, ArH), 4.00 (OCH_3 , s), 3.259 (s, 3H), 2.441 (s, 3H); ^{13}C NMR (400 MHz, CDCl_3 , δ (ppm)) δ : 10.13, 35.59, 56.07, 113.60, 116.01, 118.47, 120.16, 123.61, 124.70, 127.35, 129.31, 134.33, 148.10, 149.91, 150.44, 160.24, 160.48 ppm. The ^1H NMR and ^{13}C NMR peaks of P^5 are similar to the earlier reported data [454, 455]. The microstructures of P^5 were prepared by re-precipitation method and SDS was used as morphology directing agent. In a typical preparation, small volume of 1mM P^5 in EtOH was injected into 5 mL of continuously stirred water and aqueous SDS separately at room temperature (25°C). Clearness of the solution was gradually disappeared and a milky yellowish color appeared after gradual increase in concentration of P^5 . The solution was allowed to stand for overnight. Concentration of both P^5 and SDS were varied to synthesize various microstructures of P^5 . During the synthesis of sample-a, b, c, d, e, f, & g concentration of SDS (3.96 mM) was kept constant and the concentration of P^5 (sample-a: $19.6\mu\text{M}$, sample-b: $38.4\mu\text{M}$, sample-c: $56.6\mu\text{M}$, sample-d: $74\mu\text{M}$, sample-e: $90.9\mu\text{M}$, sample-f: $122.8\mu\text{M}$, sample-g: $166.6\mu\text{M}$,) was varied to study the effect of concentration of P^5 on aggregated microstructures. Similar method was used for the preparation of P^5 microstructures in the absence of SDS and the samples are named as sample-a₁ to g₁ respectively.

Scheme 1: Synthesis of 4-[(2-Hydroxy-3-methoxy-benzylidene)-amino]-1,5-dimethyl-2-phenyl-1,2-dihydro-pyrazol-3-one(P^5)



7.2.3. Characterization

UV-Vis spectroscopic measurements were carried out in a Shimadzu UV-1800 spectrophotometer with a 1cm quartz cuvette. Hitachi F-7000 Fluorescence Spectrophotometer was used to record the fluorescence spectra. ^1H and ^{13}C NMR spectra were recorded on a Bruker ASCEND spectrometer operating at 400MHz in CDCl_3 and deuterated dimethyl sulfoxide (DMSO-d_6). The Fourier transform infrared (FT-IR) spectra

were obtained in the range of 4000–400 cm^{-1} using KBr pellets on a PerkinElmer Spectrum-Two FTIR spectrometer. Fluorescence lifetimes were obtained by the method of Time Correlated Single-Photon Counting (TCSPC) using Horiba, DeltaFelix Modular Fluorescence Lifetime System with diode laser excitation source (372 nm) and the detection wavelength were 525 nm for P^5 hydrosol, 520 nm for P^5 with Al^{3+} and 535 nm for P^5 with Zn^{2+} . Lamp profiles were measured with a band-pass of 3 nm using Ludox as the scatterer. The decay parameters were analyzed using non-linear iterative fitting procedure based on the Marquardt algorithm [456]. The quality of fit was assessed over the entire decay, with a plot of weighted residuals and other statistical parameters e.g. the reduced χ^2 ratio [457]. The signal was collected at magic angle (54.7°) using a PPD-850, Picosecond Photon Detection Module. Time resolution of the experimental setup was ~ 80 ps. Optical microscopy is study were carried out using an NIKON ECLIPSE LV100POL upright microscope with CCD camera (model no. Nikon DS-Fi 1), polarizer-analyzer assembly and 100W mercury lamp as excitation source for emission study. Particle size distribution analysis was measured by dynamic light scattering (DLS) experiments on a Malvern Zetasizer Nano ZS90 instrument.

7.2.4. Limit of Detection (LOD)

The LOD was calculated on the basis of the fluorescence titration. Standard deviation of the blank measurement was obtained from the plot of fluorescence intensity of P^5 as a function of its increasing concentrations. This procedure was repeated five times to get its average. The slopes (k) of 3σ method for sensing Al^{3+} and Zn^{2+} by P^5 was obtained from the plot of P^5 PL emission intensity as a function of increasing Al^{3+} & Zn^{2+} concentrations at 520 nm and 535 nm respectively. The detection limit was calculated using the following equation [458].

$$\text{LOD} = 3\sigma/k$$

Where, σ is the standard deviation of blank measurement, and k is the slope of the calibration curve obtained from linear dynamic plot of fluorescence intensity versus increasing concentration of metal ions.

7.2.5. Fluorescence Quantum Yield

We also measured the fluorescence quantum yield of P^5 , $\text{P}^5\text{-Al}^{3+}$ and $\text{P}^5\text{-Zn}^{2+}$ in ethanol and P^5 aggregates in water using the following equation, where quinine sulphate was used as standard with $\lambda_{\text{ex}}=350$ nm.

$$\Phi_s = \Phi_r (A_r F_s / A_s F_r) (\eta_s^2 / \eta_r^2)$$

A_s and A_r are the absorbance of the sample and reference solutions, respectively, at the same excitation wavelength, F_s and F_r are the corresponding relative integrated fluorescence intensities, η_s and η_r are the refractive index of the sample and reference respectively.

7.3. Results and discussion

Synthesis of **P⁵** is depicted in Scheme 1 and synthesis details are described in Experimental Section. It was completely characterized by physicochemical and spectroscopic analysis. The ¹H NMR (Fig. 7.1) and ¹³C NMR (Fig. 7.2) spectra were recorded to confirm the purity and the structure of the probe. IR (Fig. 7.3) spectrum shows a vibration band at 1598 cm⁻¹ which can be assigned to stretching vibrational mode of imine (–CH=N–) group present in the **P⁵** molecules.

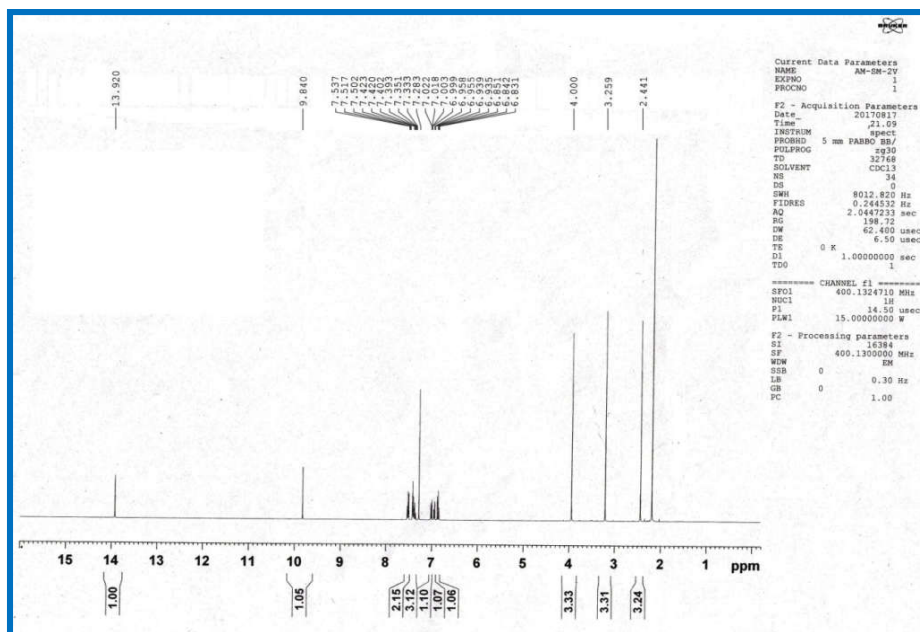


Fig. 7.1: ¹H-NMR spectra of **P⁵** in CDCl₃.

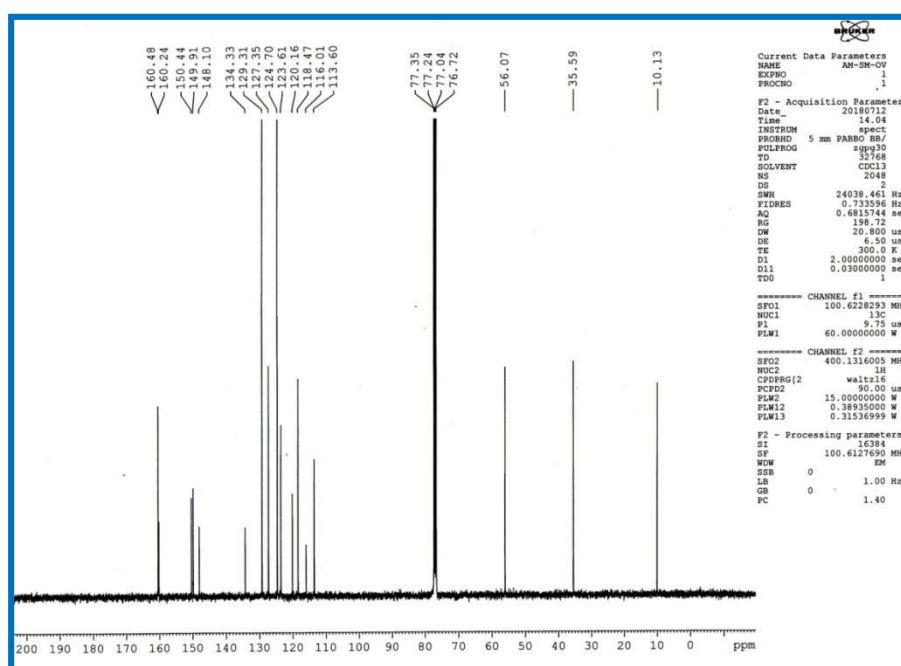


Fig. 7.2: ¹³C-NMR spectra of **P⁵** in CDCl₃

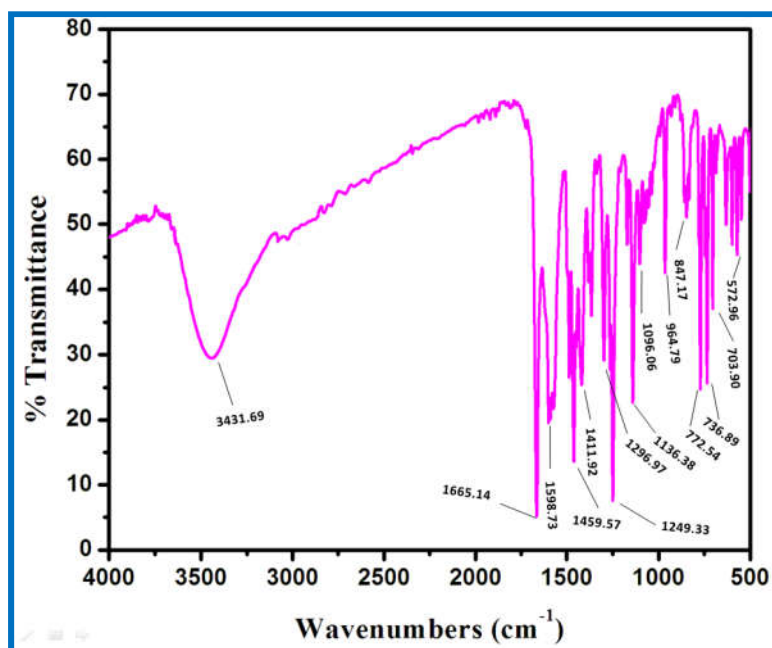


Fig. 7.3: FT-IR of chemosensor P^5 .

7.3.1. Aggregation-induced Emission Enhancement (AIEE)

7.3.1.1. Optical microscopic study

Morphologies of the particles as observed by fluorescence microscopy are shown in **Fig. 7.4**. At lower concentration of P^5 bar shaped morphologies are clearly observed for the sample-e, f, g. On the other hand, one dimensional growth of the microcrystal is observed with increasing concentration of P^5 . P^5 shows rod-shaped microstructures with greenish yellow emission upon UV excitation. There is a clear indication that dimension of the particles increases along its length with increasing concentration of P^5 .

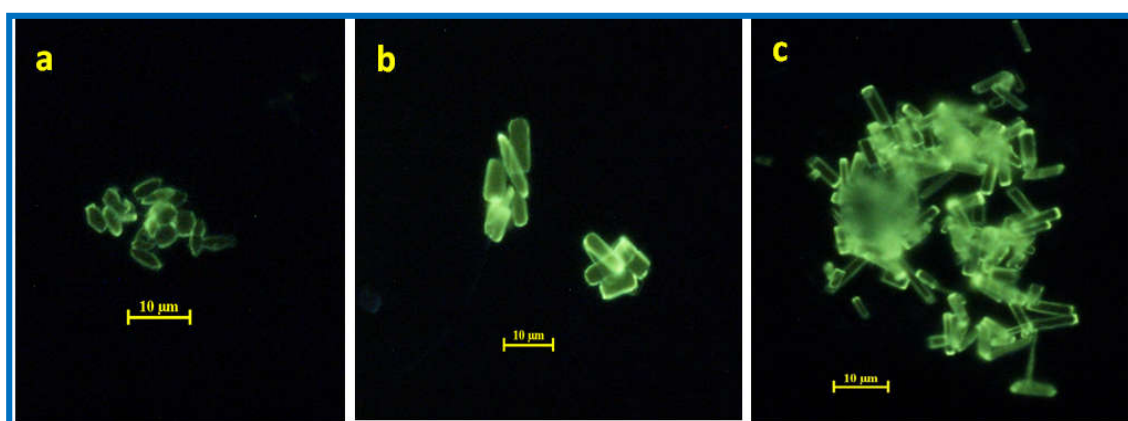


Fig. 7.4: Optical fluorescence microscopy images (under UV excitation) of P^5 microstructure prepared in presence of 4 mM SDS (a) sample-e, (b) sample-f (c) sample-g .

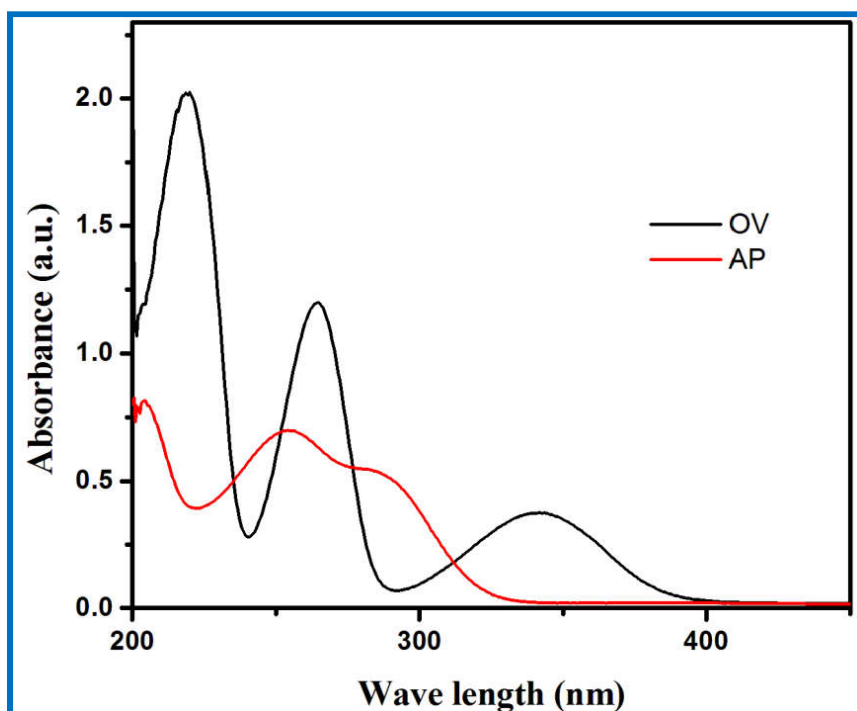


Fig. 7.5: UV-Vis spectra of O-Vanillin (OV) and 4-aminoantipyrine (AP) in EtOH.

7.3.1.2. UV-Vis Study

UV-Vis absorption spectra of P^5 in EtOH and the as prepared hydrosol of P^5 (sample a, b, c, d, e, f) are shown in **Fig. 7.8**. The UV-Vis absorption spectrum of P^5 in EtOH has two distinct regions at 210-280 nm and 300-400 nm respectively. Comparison of UV-Vis spectra of P^5 with that of vanillin and antipyrine moieties in ethanol (**Fig. 7.5**) suggests that the structured absorption bands in the region 210-280 nm are due to aromatic π - π^* absorption band of O-vaniline and antipyrine group present in P^5 . In order to understand the nature of absorption band at 300-400 nm, we did the UV-Vis absorption study of P^5 and O-vaniline in presence of base (**Fig. 7.6**). Gradual increase of base concentration (pH= 8 to 11), a new red shifted broad absorption band ($\lambda_{\text{max}} = 390$ nm) for P^5 appear with an isosbestic point at 372 nm (**Fig. 7.6a**). Similarly, absorption study of O-vaniline (**Fig. 7.6b**), and comparison with P^5 reveals that the broad absorption band of P^5 at 300-400 nm is due to intramolecular proton transfer absorption band between phenolic-OH and iminine N atom in P^5 .

However, with gradual increase of water fraction, aggregation starts and the absorption maximum at 332 nm diminishes (**Fig. 7.7**). On the other hand, a new shoulder band at ~264 nm is appeared and the absorbance of the band increases with increasing volume percentage of water. In addition, the overall shift of the spectral baseline of samples a-f relative to the monomer (**Fig. 7.8**) is attributed to the scattering of light by the larger aggregated structures in solution.

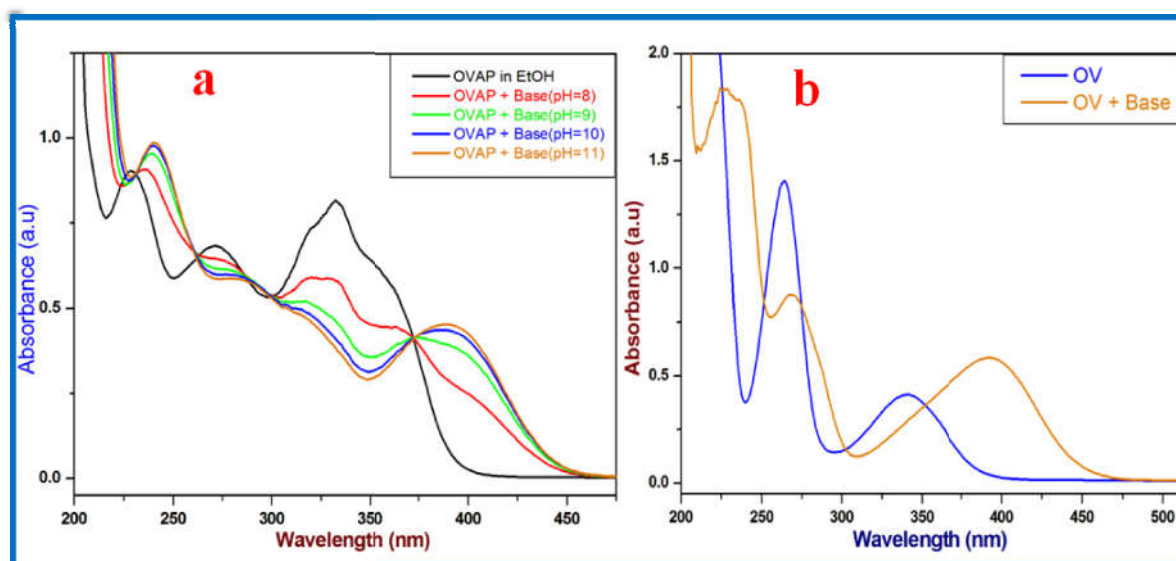


Fig. 7.6: UV-Vis absorption spectra of (a) P^5 with increasing PH (b) o-vaniline (OV) in the absence and presence of base (pH = 10)

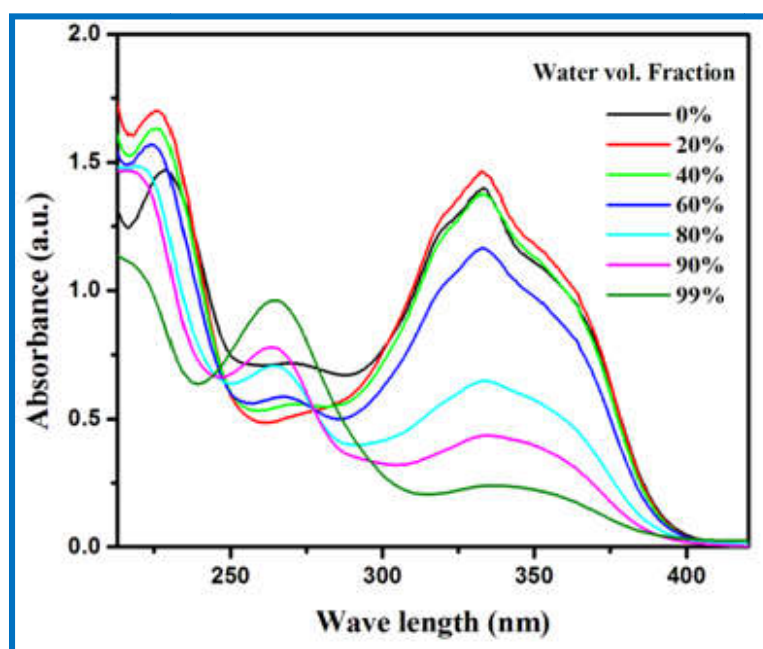


Fig. 7.7: UV-Vis absorption spectra of P^5 in (i) 0% water (OVAP in EtOH), (ii) 20% water, (iii) 40% water, (iii) 60% water, (iv) 80% water, (v) 90% water and (vi) 99% water.

7.3.1.3. Emission Study

PL spectra of P^5 in EtOH and its aggregated hydrosol (in 4mM SDS) with different amount of P^5 are shown in (Fig. 7.9a). It is observed that the dilute solution (6 μ M) of P^5 in EtOH exhibits very weak broad emission band with peak maximum at 550 nm upon photo excitation at 360 nm. But the aggregated hydrosol of P^5 in SDS (4 mM) medium exhibits nearly 25 nm blue shifted intense structured emission with a maximum at 525 nm. It is also observed that the fluorescence intensity of P^5 hydrosol in the region 475-650 nm increases gradually with the increasing concentration of P^5 .

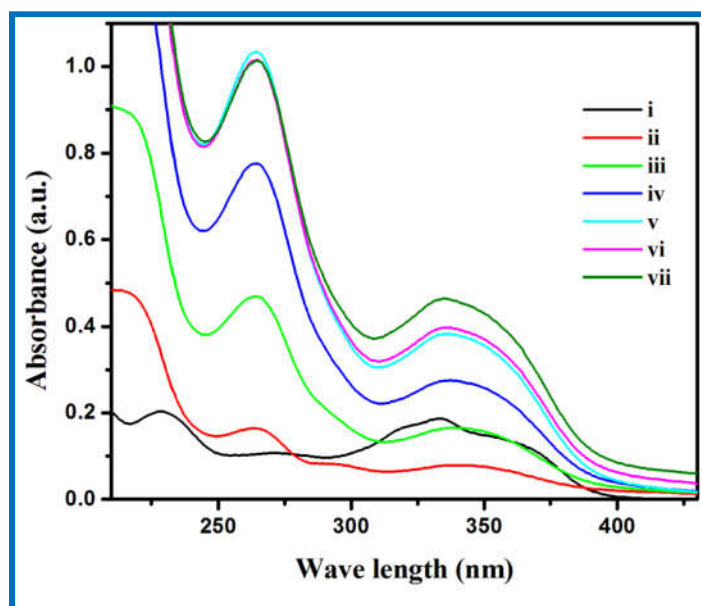


Fig. 7.8: The UV-Vis absorption spectra of (i) P^5 in EtOH (ii) sample-a, (iii) sample-b, (iv) sample-c, (v) sample-d, (vi) sample-e, (vii) sample-f.

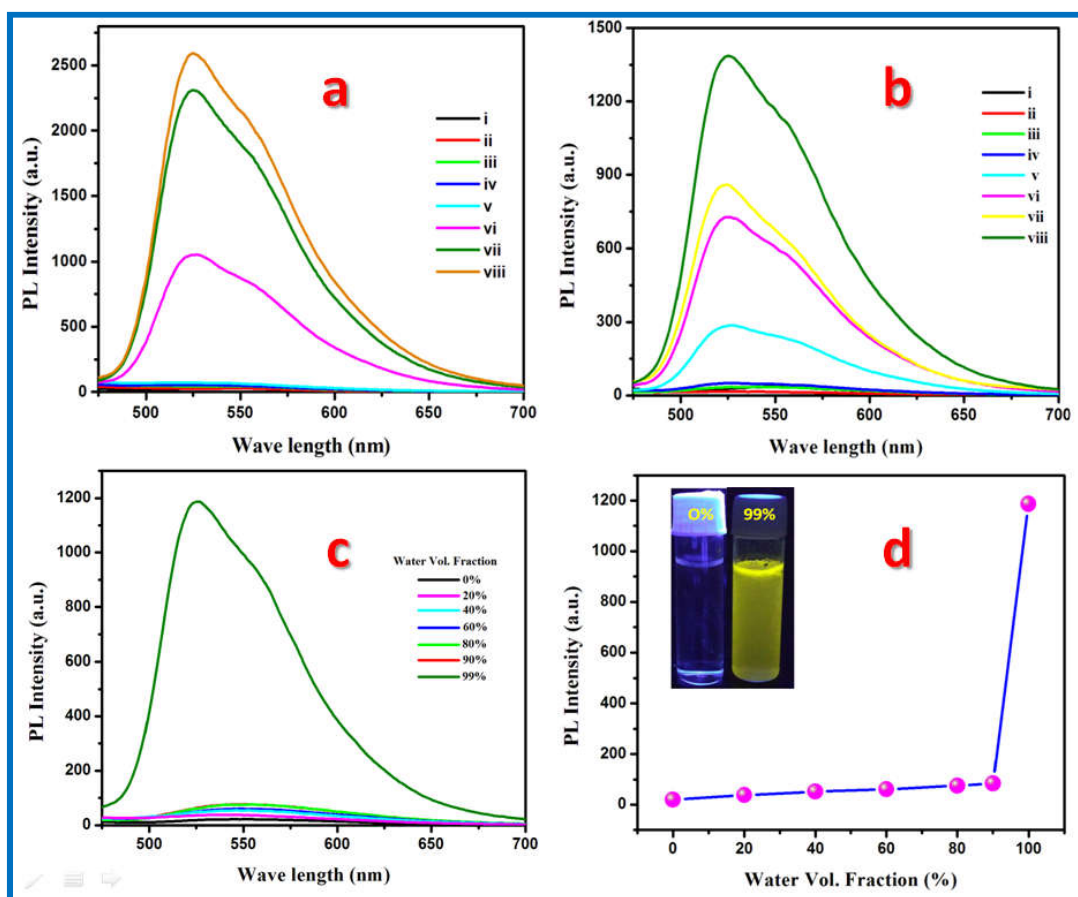


Fig. 7.9: (a) Fluorescence emission spectra of (i) P^5 in EtOH, P^5 hydrosol prepared in the presence of 4 mM SDS (ii) sample-a, (iii) sample-b, (iv) sample-c, (v) sample-d, (vi) sample-e, (vii) sample-f, (viii) sample-g, (b) The Fluorescence emission spectra of P^5 hydrosol prepared in the absence of SDS (i) P^5 in EtOH (ii) sample-a₁, (iii) sample-b₁, (iv) sample-c₁, (v) sample-d₁, (vi) sample-e₁, (vii) sample-f₁, (viii) sample-g₁. All emission spectra were taken with 360 nm excitation. Inset

Fluorescence images of P^5 in EtOH and its aggregated hydrosol under illumination of 366 nm radiation. (c) Emission spectra of freshly prepared P^5 (62 μM) in 0% -99.9% water. λ_{exc} : 360 nm. (d) Plot of relative variation of PL intensity against water content (fw) in the EtOH/water mixture. Insets: Fluorescence images of P^5 (0% and 99% H₂O) under 366 nm illuminations.

This is due to aggregation-induced emission enhancement (AIEE) effect. Energy optimized structure of P^5 (**Fig. 7.10**) suggests that the molecule P^5 as a whole is floppy in nature. Now upon aggregation in its aggregated hydrosol, the floppiness of the molecule decreases, resulting the restriction of intramolecular rotation (RIR) to be operative to show AIEE emission. Also a similar observation in PL study using different concentration of P^5 without SDS is shown in **Fig. 7.9b**. It shows that the PL intensity of the aggregated hydrosol of P^5 without SDS is lower compared to the hydrosol in SDS medium.

Fig. 7.9c shows the fluorescence emission spectra of P^5 at different volume fractions of water for a fixed concentration of P^5 (47 μM). It is observed that PL intensity increases gradually up to 90% water fraction, indicating the fabulous AIEE properties of P^5 . But a sharp change of PL spectra with increased intensity are observed as the volume percentage of water changes from 90% to 99%. PL spectrum of the aggregated hydrosol at 99% v/v is blue shifted and it is due to comparatively less polar environment faced by P^5 in its aggregated state. A plot of PL emission intensity as a function of volume fraction of water is show in **Fig. 7.9d** and it shows a sharp rise in PL intensity at > 90% volume fraction of water. On the other hand, we also measured the solid state emission of P^5 which is similar to that of the aggregated hydrosol of P^5 (**Fig. 7.11**).

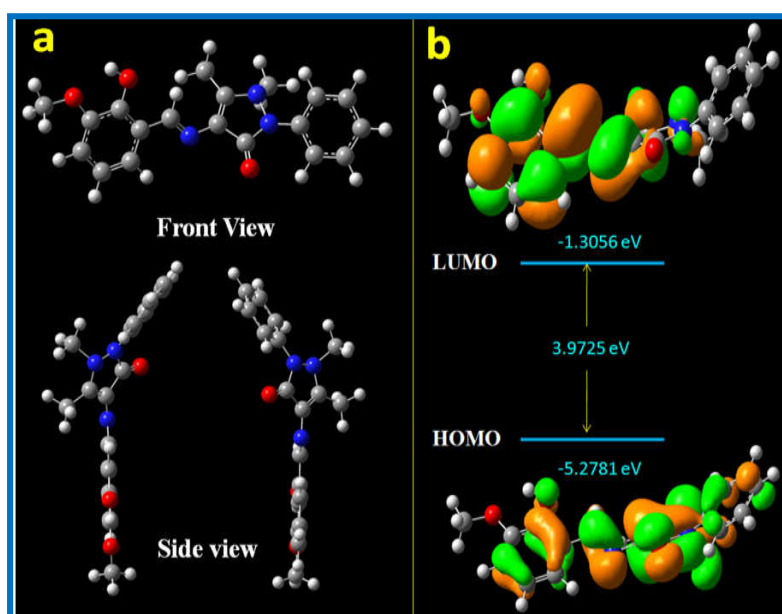


Fig. 7.10: a) Optimized structure of P^5 . b) Frontier molecular orbital plots of HOMO and LUMO energy levels of P^5 calculated by using DFT-B3LYP/6-31 G (d,p) level of theory as implemented on Gaussian 09.

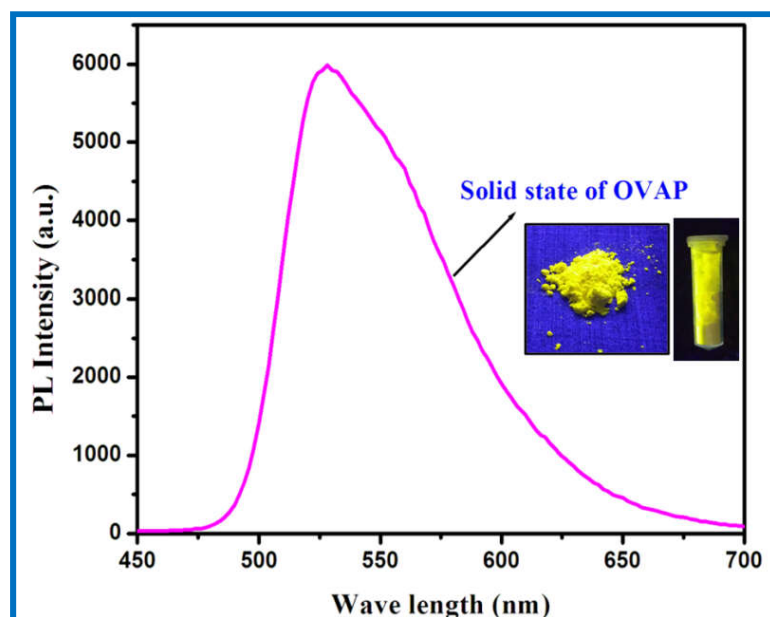


Fig. 7.11: Solid state emission of P^5 , (Ex-360 nm).

7.3.1.4. Time-Resolved Photoluminescence (TRPL) Measurements

In order to understand the photophysical behaviour time resolved photoluminescence (TRPL) were carried out as shown in **Fig. 7.12**. Measurement of fluorescence lifetime is more robust than measurement of fluorescence intensity, because it depends neither on the excitation photon density nor on the concentration of the fluorophore. **Fig. 7.12** shows the fluorescence decay of P^5 in pure EtOH and EtOH-H₂O (99%) mixture. Analysis of fluorescence decay curve shows that the fluorescence lifetime value increases from 96 ps for P^5 in EtOH to 1.72 ns for P^5 aggregates in 99% volume fraction of water. The measured emission quantum yield of P^5 in EtOH and aggregated hydrosol of P^5 are $\Phi_{OVAP}(\text{EtOH}) = 0.009$ and $\Phi_{OVAP}(\text{agg}) = 0.172$ respectively. On the basis of radiative rate constant (K_r) and emission quantum yield, we have calculated the non-radiative rate constant (K_{nr}) and the values are listed in **Table 1**. There is almost 21 times decreased of K_{nr} value took place upon aggregation of P^5 . Thus the increased PL lifetime of P^5 aggregates is the results of decreases of non-radiative process due to restrictions of intramolecular rotational (RIR) motion upon aggregation.

7.3.1.5. DLS Measurement

DLS measurements were also performed in support of average particle size distribution of P^5 aggregates in the presence of 99% water volume fraction in H₂O/EtOH mixture (**Fig. 7.13**). DLS studies revealed that the diameter of the aggregated particles lies between 200 nm to 400 nm and the average calculated diameter of P^5 aggregates is found to be ~310nm and this is in the range of previously reported many other AIEE systems [433,434].

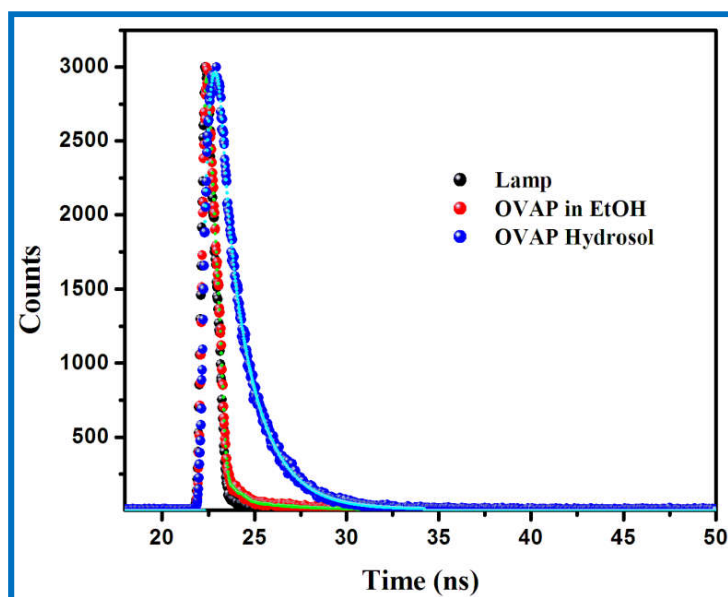


Fig. 7.12: (a) Time-resolved fluorescence spectra of P^5 (0% water; red), P^5 (99% water; blue) and Lamp (black). (b) Time resolved fluorescence spectra of P^5 (47 μM) and different metal of Al^{3+} and Zn^{2+} in EtOH respectively. Lamp (black), P^5 in EtOH (red), 1: 1 equiv Al^{3+} (blue), 1:1 equiv Zn^{2+} (pink), ($\lambda_{\text{exc}} = 372 \text{ nm}$, $\lambda_{\text{em}} = 520 \text{ nm}$ for Al^{3+} and 535 nm for Zn^{2+}).

Table 1: Photophysical parameters of P^5 , Al- P^5 , Zn- P^5 and aggregated P^5

Sample	τ_f (avg. ns)	Φ_f	K_r (S^{-1}) (Φ_f / τ_f)	K_{nr} (S^{-1}) [($1/\tau_f$) - K_r]	χ^2
OVAP in EtOH	0.096	0.009	0.093	10.32	1.27
Aggregated OVAP (99% H_2O)	1.72	0.172	0.1	0.48	1.12
OVAP+ Al^{3+} (1:1) in EtOH	2.23	0.68	0.304	0.14	1.13
OVAP+ Zn^{2+} (1:1) in EtOH	2.32	0.47	0.202	0.22	1.11

7.3.2. Analytical Performance: Sensing Knack toward Al^{3+} & Zn^{2+} Ions

7.3.2.1. UV-Vis Spectroscopic Studies of OVAP in the Presence of Metal Ions

Interaction of P^5 with various metal ions (Na^+ , K^+ , Ag^+ , Mg^{2+} , Ca^{2+} , Co^{2+} , Ni^{2+} , Cu^{2+} , Cd^{2+} , Zn^{2+} , Pb^{2+} , Hg^{2+} , Cr^{3+} , Fe^{3+} , Al^{3+} and Mn^{2+}) was performed in EtOH medium. The absorption spectrum of chemosensor P^5 exhibits two weak absorption bands at 229 nm and 272 nm, a broad band at 334 nm originating due to intramolecular proton transfer absorption of P^5 (**Fig. 7.14**). The position of absorption band remained unchanged with most of the metal ions (1 equivalents of each) except Al^{3+} , Co^{2+} , Cu^{2+} , Ni^{2+} , Cd^{2+} , Mn^{2+} and Zn^{2+} where a broad absorption peak appear at $\sim 400\text{-}470 \text{ nm}$ with a concomitant decreases of 334 nm band.

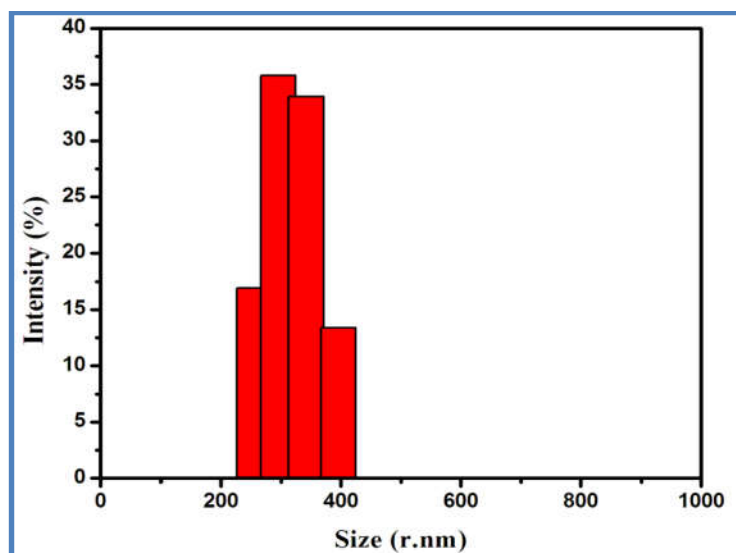


Fig. 7.13: Particle size distribution of P^5 (47 μM) in mixed aqueous media of 99% water content determined by DLS measurements.

Titration experiments with gradual addition of Al^{3+} & Zn^{2+} ions resulted in diminishing of the peaks at 229, 272 and 334 nm along with the appearance of a new peak at 406 nm for Al^{3+} and 425 nm for Zn^{2+} (**Fig. 7.14**), and these new peaks are attributed to the strong ligand-to-metal charge-transfer (LMCT) absorption band. The presence of isobestic points at 380 and 250 nm established the transformation of a free receptor to its aluminium complex as shown in **Fig. 7.14a**. Titration experiments with Zn^{2+} also yielded almost similar results as in the case of Al^{3+} (**Fig. 7.14b**). Interestingly, a colour change from colourless to light yellow and deep yellow was observed with Al^{3+} and Zn^{2+} , respectively (inset **Fig. 7.14a** and **Fig. 7.14b**). Job's plot obtained from the titration experiments yielded 1 : 1 stoichiometry of the complex between P^5 and each of metal ions Al^{3+} & Zn^{2+} (**Fig. 7.15a** & **7.15b**) respectively.

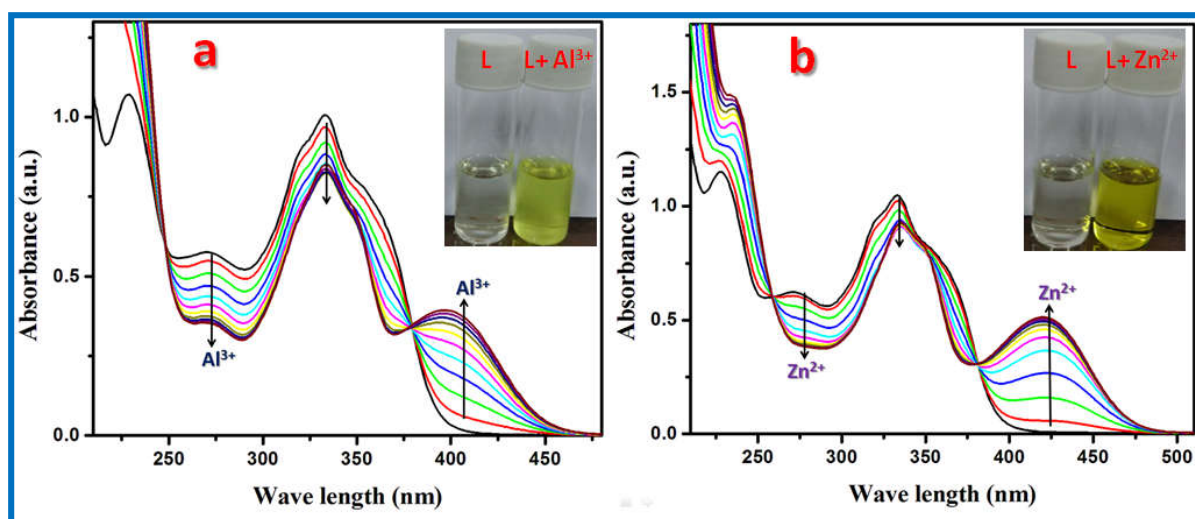


Fig. 7.14: Changes in absorption spectra of P^5 ($47\mu\text{M}$) with (a) the incremental addition of Al^{3+} . Inset: colour change upon the addition of Al^{3+} and Zn^{2+} to P^5 , (b) the incremental addition of Zn^{2+} .

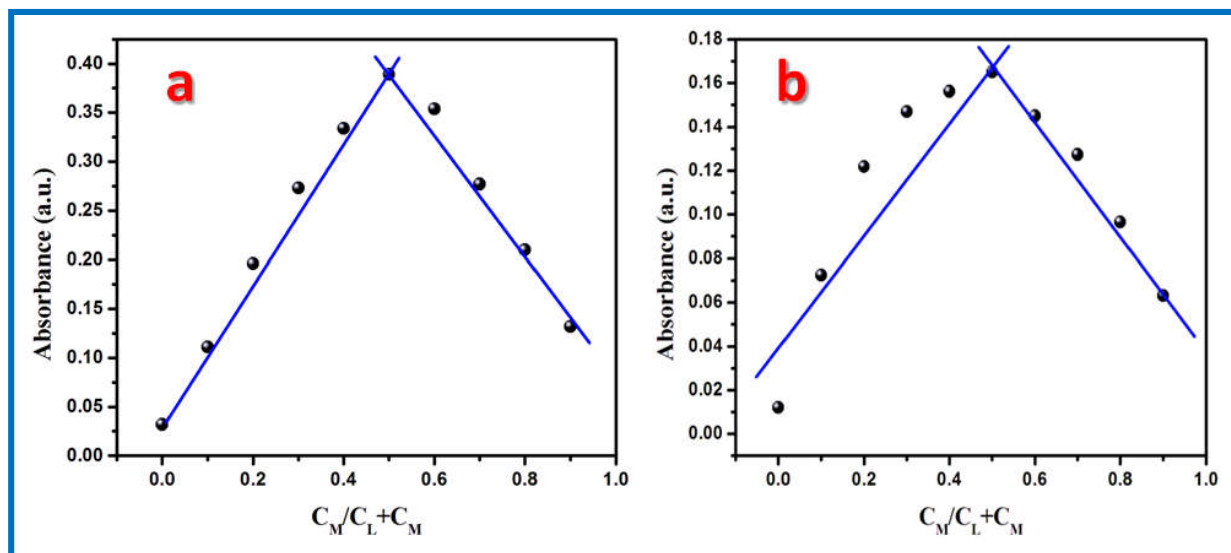


Fig. 7.15: Job's plot of OVAP according to the method for continuous variations, indicating the 1:1 stoichiometry for (a) OVAP– Al^{3+} (b) OVAP– Zn^{2+} .

7.3.2.2. Fluorescence Spectroscopic Studies of P^5 in the Presence of Metal Ions

PL spectra of P^5 in presence of various metal ion in solution are shown in **Fig. 7.16**. P^5 displays a weak emission peak at 550 nm when the excitation wavelength is 360 nm. In the presence of various metal ions (Na^+ , K^+ , Ag^+ , Mg^{2+} , Ca^{2+} , Co^{2+} , Ni^{2+} , Cu^{2+} , Cd^{2+} , Zn^{2+} , Pb^{2+} , Hg^{2+} , Cr^{3+} , Fe^{3+} , Al^{3+} , Mn^{2+} in ethanolic solution), a remarkable enhancement of the emission spectra of P^5 was observed only with Al^{3+} and Zn^{2+} peaking at two distinct wavelengths corresponding to 520 nm and 535 nm, respectively (**Fig. 7.16a** & **7.16b**). Green fluorescence was observed in the case of Al^{3+} whereas yellowish green fluorescence was observed in presence of Zn^{2+} (inset **Fig. 7.16a** & **7.16b**). These results also validated the selectivity of P^5 towards Al^{3+} and Zn^{2+} . Fluorescence Titration experiments were also carried out with gradual addition of Al^{3+} and Zn^{2+} to the solution of P^5 . In both the cases, a gradual increase in the emission intensity of P^5 in presence of metal ions (Al^{3+} & Zn^{2+}) was observed (**Fig. 7.16**). Relative fluorescence colour changes of P^5 in presence of Al^{3+} and Zn^{2+} are shown in the inset of **Fig. 7.16a** & **7.16b** respectively. We have also carried out fluorescence titration using the equimolar mixture of Al^{3+} and Zn^{2+} (**Fig. 7.17**). Two distinct emission maxima (520 nm & 535 nm) though separated by only 15 nm are observed and it further supports that P^5 can be an efficient fluorescence probe for simultaneous sensing of Al^{3+} and Zn^{2+} in a mixture.

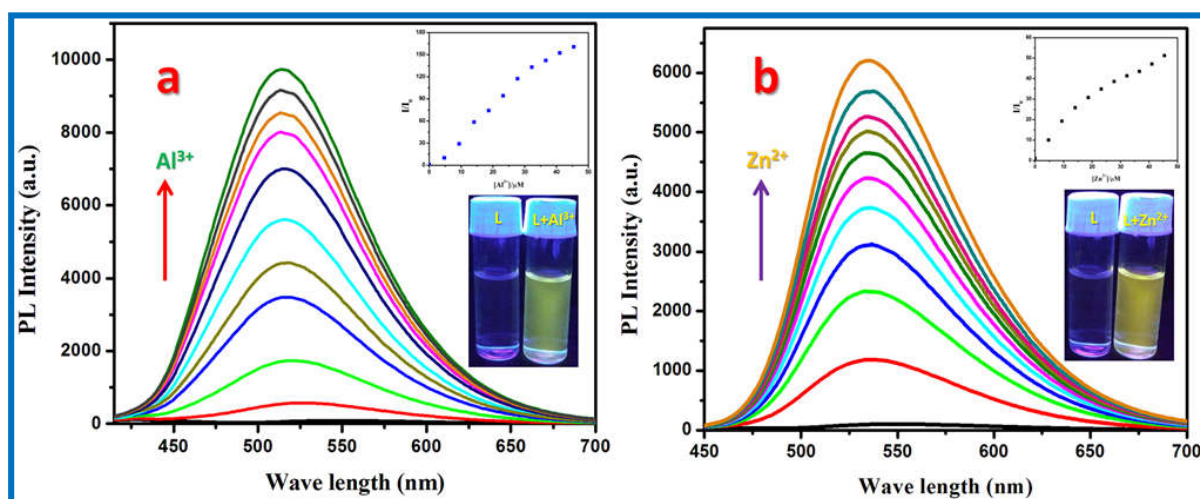


Fig. 7.16: (a) Changes in emission spectra of P^5 ($47\mu\text{M}$) (a) with the incremental addition of Al^{3+} . [Inset: intensity at 520 nm vs. $[\text{Al}^{3+}]$ plot, visible colour change upon the addition of Al^{3+} to P^5 under UV lamp] ($\lambda_{\text{ex}} = 360$ nm). (b) With incremental addition of Zn^{2+} , [Inset: intensity at 535 nm vs. $[\text{Zn}^{2+}]$ plot, visible colour change upon the addition of Zn^{2+} to P^5 under UV lamp].

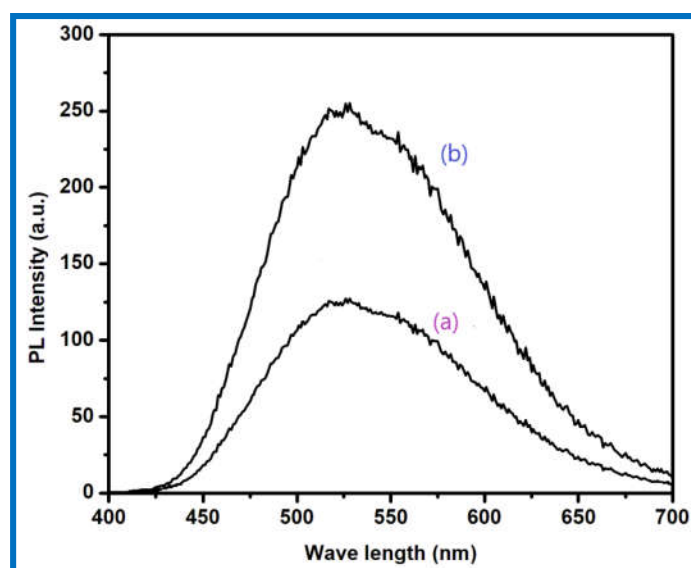


Fig. 7.17: Fluorescence emission spectra of P^5 (60 mM) in presence of (a) 20 mM each of Al^{3+} & Zn^{2+} , (b) 40 mM each of Al^{3+} & Zn^{2+} .

7.3.2.3. Time-Resolved Photoluminescence (TRPL) Study

The TRPL measurements also carried out to better understand the mechanism of the ‘turn-on’ emission responses of P^5 toward Al^{3+} and Zn^{2+} ion as shown in **Fig. 7.18**. The fluorescence lifetime (τ) of P^5 in EtOH is 96 ps, whereas longer average fluorescence lifetimes of 2.23 ns and 2.32 ns were detected in the presence of 1:1 equiv of Al^{3+} & Zn^{2+} respectively. Our measured fluorescence quantum yield for P^5 , $P^5\text{-Al}^{3+}$ and $P^5\text{-Zn}^{2+}$ in EtOH are 0.009, 0.68 and 0.47 respectively (**Table 1**). We further calculate the non-radiative rate

constant of P^5 and its complex with Al^{3+} & Zn^{2+} (Table 1). On the basis of the measured fluorescence quantum yield and fluorescence lifetime, the non-radiation rate constant of P^5 in EtOH, P^5 hydrosol, P^5-Al^{3+} and P^5-Zn^{2+} were obtained as 10.32, 0.48, 0.14 and 0.22 S^{-1} respectively. The K_{nr} value upon complexation decreases nearly 73 time in P^5-Al^{3+} and 47 times in P^5-Zn^{2+} complex. Thus the enhance fluorescence lifetime is due to possible decreases of K_{nr} upon chelation between metal ions and P^5 .

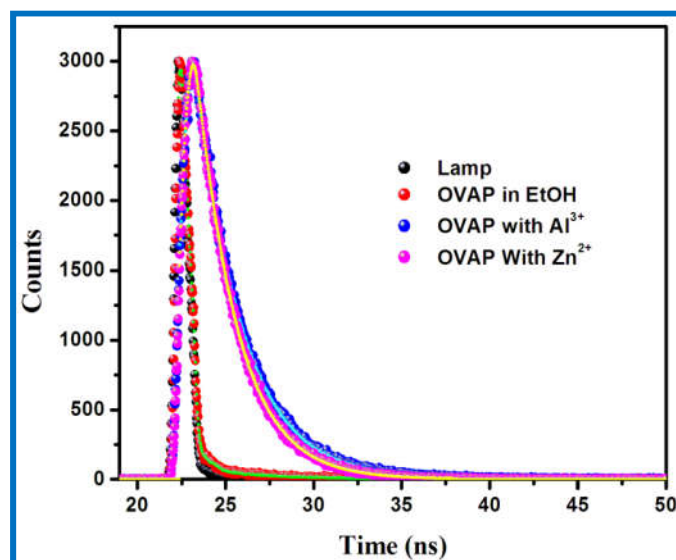


Fig. 7.18: Time resolved fluorescence spectra of P^5 (47 μM) in EtOH and P^5 with Al^{3+} & Zn^{2+} respectively. Lamp (black), P^5 in EtOH (red), 1: 1 equiv P^5 & Al^{3+} (blue); 1:1 equiv P^5 & Zn^{2+} (pink); ($\lambda_{ex} = 372$ nm, $\lambda_{em} = 520$ nm for Al^{3+} & P^5 and 535 nm for Zn^{2+} & P^5).

7.3.2.4. Metal Ion Competition Studies

The selectivity of P^5 towards Al^{3+} and Zn^{2+} was also established through experiments in the presence of competing metal ions (Fig. 7.19) through UV-Vis and fluorescence emission study. As seen in Fig. 7.19a, the absorption spectrum of chemosensor P^5 shows two weak absorption bands at 272 and 334 nm. The position of absorption band remained unchanged with most of the metal ions except Al^{3+} , Co^{2+} , Cu^{2+} , Zn^{2+} , Ni^{2+} , Cd^{2+} , Mn^{2+} where a new broad band ~400-470 nm is appeared. It is interesting to note that among all the tested metal ions only Al^{3+} and Zn^{2+} rendered significant fluorescence ‘turn-on’ responses, whereas other relevant competing metal ions has no noteworthy effect in the emission spectra (Fig. 7.19b). In order to establish the specific selectivity of P^5 toward Al^{3+} and Zn^{2+} , we also carried out the single and dual metal competitive analysis (Fig. 7.20 & 7.21). Bar diagram plot for the measurement of selectivity of P^5 for Al^{3+} , Zn^{2+} ions in the presence of other competitive metal ions are shown in Fig. 7.22. The photographs of P^5 with different metal

ions (under normal light and UV light irradiations) well-verified its sensitivity by strong blue fluorescence as depicted in *Fig. 7.23*.

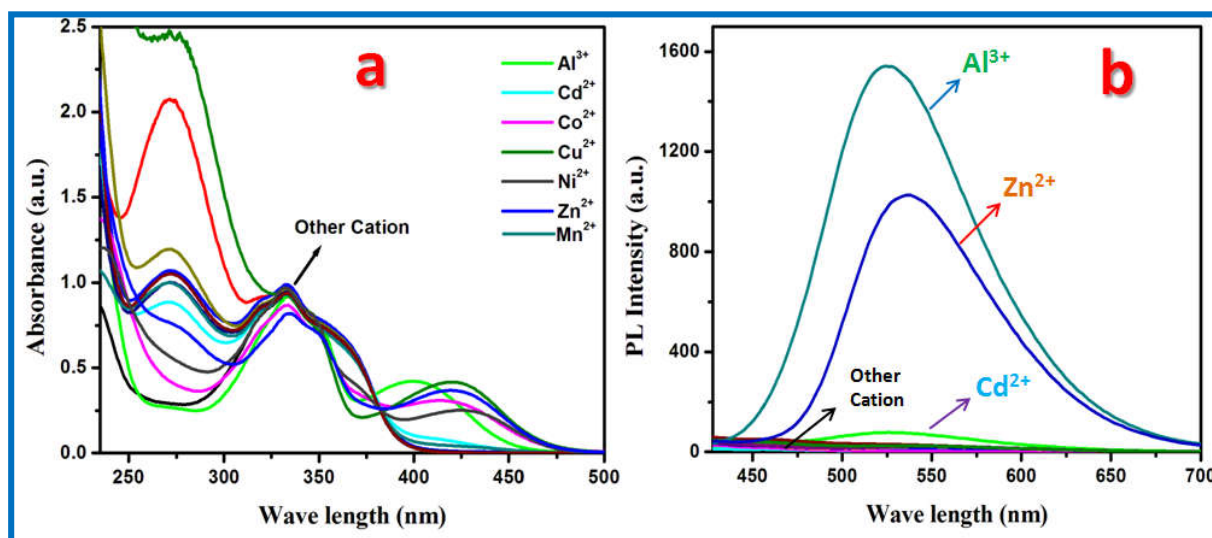


Fig. 7.19: a) UV-Vis absorption spectra of antipyrene chemosensor P^5 (47 μ M) in the absence and presence of different metal ions (45 μ M) at 25 $^{\circ}$ C. b) Fluorescence emission spectra of P^5 (47 μ M) in Ethanol in the presence of different metal ions (45 μ M) such as Na^+ , K^+ , Ag^+ , Mg^{2+} , Ca^{2+} , Co^{2+} , Ni^{2+} , Cu^{2+} , Cd^{2+} , Zn^{2+} , Pb^{2+} , Hg^{2+} , Cr^{3+} , Fe^{3+} , Al^{3+} and Mn^{2+} . Excitation wavelength was at 360 nm.

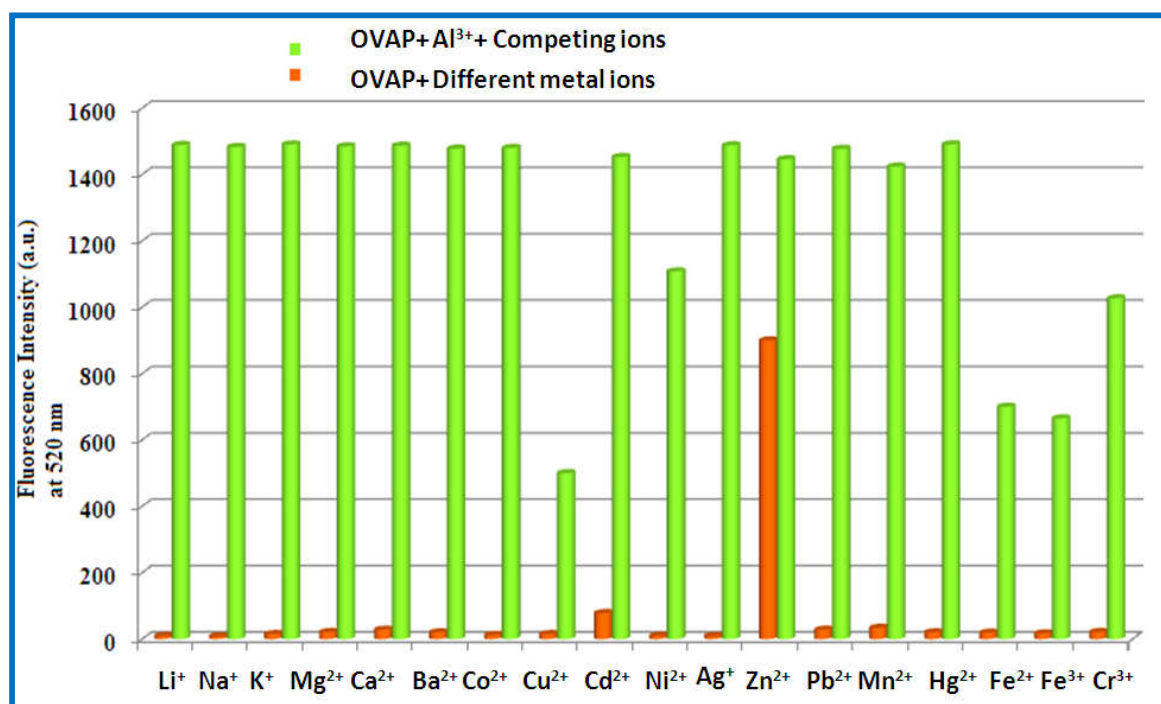


Fig. 7.20: Selectivity of P^5 for Al^{3+} ions in the presence of other competitive metal ions, excitation wavelength and emission maximum are 360 nm and 520 nm, respectively. Orange bars represent fluorescent intensity after the addition of the appropriate metal ion in a 47 μ M solution of P^5 . Light green bars represent the subsequent addition of same equiv. of Al^{3+} ions in each of the samples.

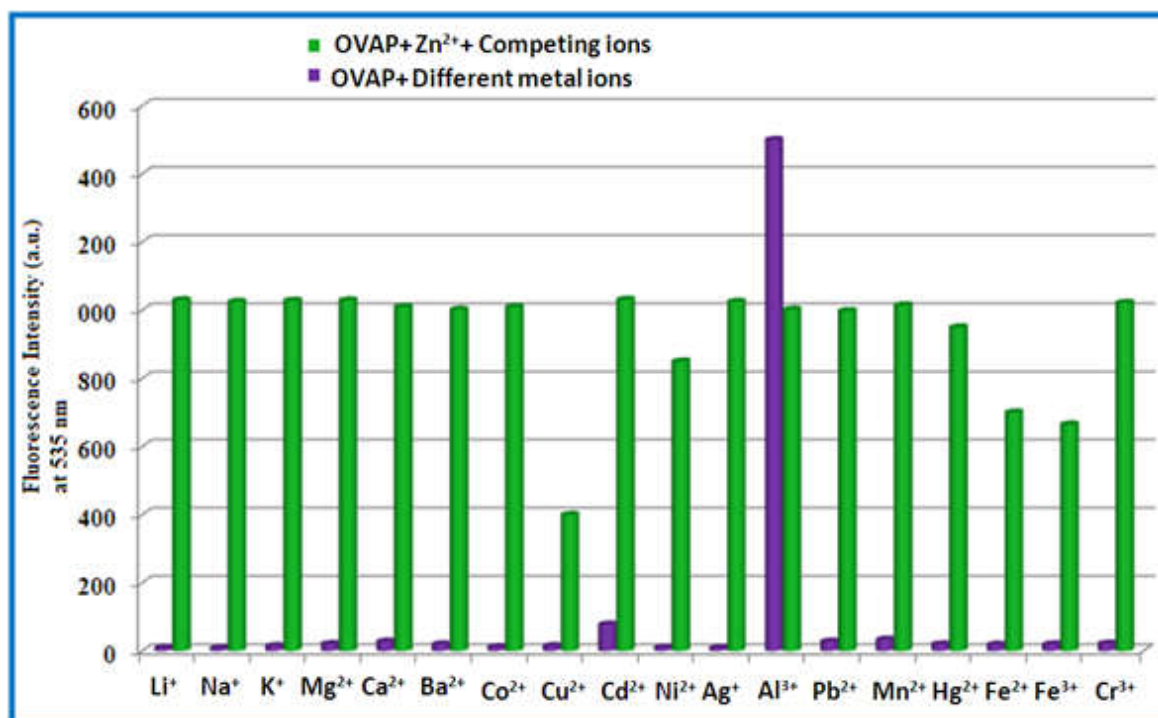


Fig. 7.21: Selectivity of P^5 for Zn^{2+} ions in the presence of other competitive metal ions, excitation wavelength and emission maximum are 360 nm and 535 nm, respectively. Violet bars represent fluorescent intensity after the addition of the appropriate metal ion in a 47 μ M solution of P^5 . Green bars represent the subsequent addition of same equiv. of Zn^{2+} ions in each of the samples.

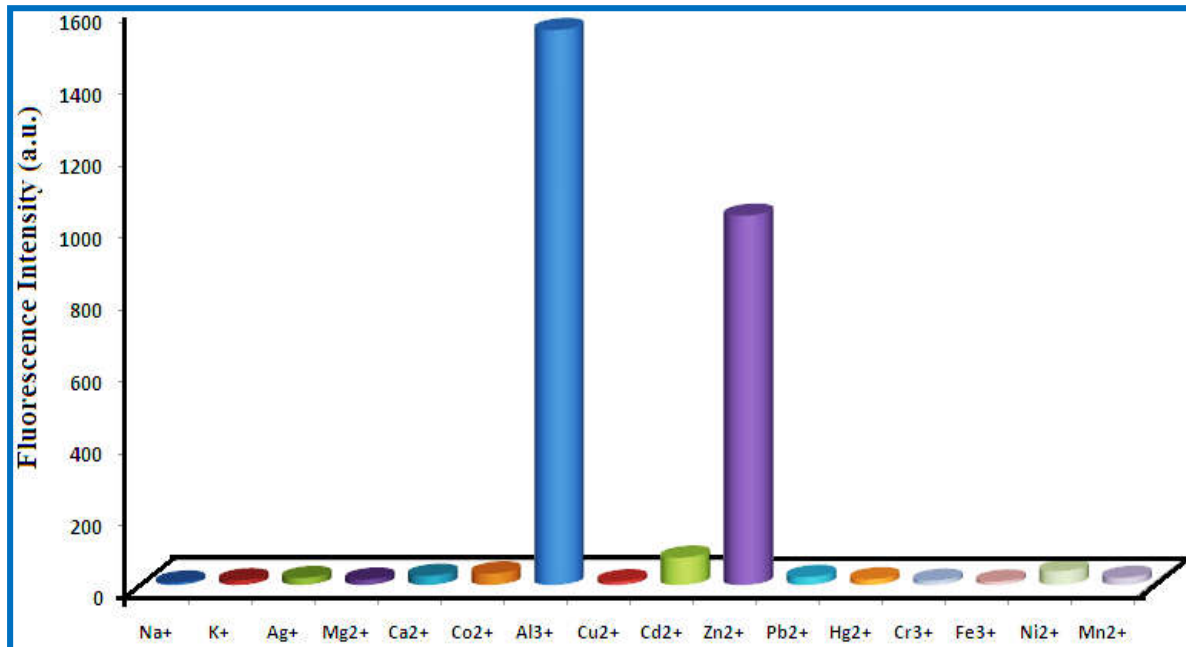


Fig. 7.22: Selectivity of P^5 for Al^{3+} , Zn^{2+} ions in the presence of other competitive metal ions, excitation wavelength 360 nm and emission maximum 520 nm for Al^{3+} and 535 nm for Zn^{2+} respectively.

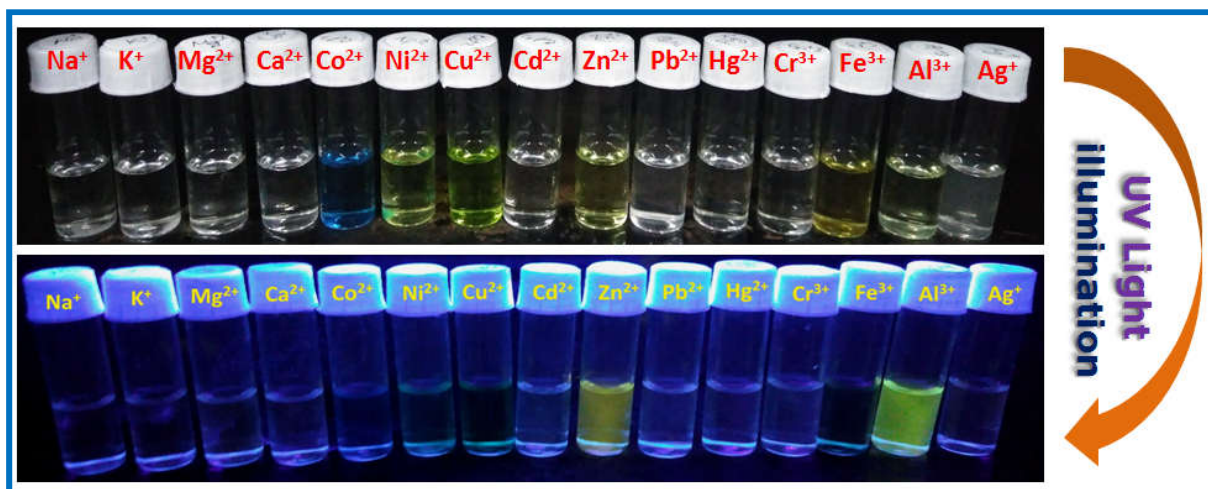


Fig. 7.23: Visual color change observed with addition of different metal ions to P^5 as seen under daylight (upper) and UV light (lower) ($\lambda = 365$ nm).

7.3.2.5. Dissociation Constant:

The dissociation constant (K_d) of the corresponding P^5 compounds with Al^{3+}/Zn^{2+} have been determined by fitting the absorption data as a function of metal ion concentration using the following equation [459],

$$I = I_0 + (I_{lim} - I_0)/2C_0 [C_0 + C_M + K_d - [(C_0 + C_M + K_d)^2 - 4C_0C_M]^{1/2}] \text{-----}(1)$$

where I_0 and I are the absorbance of P^5 at 406 nm in the absence and presence of Al^{3+} and at 425 nm in the absence and presence of Zn^{2+} respectively; C_0 is the total concentration of P^5 , C_M is the concentration of metal ion i.e Al^{3+} or Zn^{2+} ; I_{lim} is the limiting value of the absorption intensity in the presence of excess metal ion. The evaluated K_d values using absorption spectral studies for Al^{3+} and Zn^{2+} are $(1.07 \pm 0.06) \times 10^{-5}$ M and $(6.16 \pm 0.47) \times 10^{-6}$ M respectively (**Fig. 7.24**). K_d values of the corresponding divalent ions with P^5 have also been obtained by the non-linear fitting of corresponding fluorescence intensity at 520 nm for Al^{3+} and 535 nm for Zn^{2+} using similar type of equation where fluorescence intensity is used instead of absorption value in equation-1 and the values are $(1.06 \pm 0.14) \times 10^{-5}$ M for Al^{3+} and $(2.53 \pm 1.71) \times 10^{-6}$ M for Zn^{2+} respectively (**Fig. 7.25**). Our observed K_d values obtained from both absorption and emission data are in excellent agreement and it proves the self consistency of our spectral data.

7.3.2.6. Detection Limit

Sensitivity of the probe are examined by measuring limit of detection (LOD) for each cation. LOD has been determined by following the 3σ method. The LOD values are 1.05 nM for Al^{3+} , 2.35 nM for Zn^{2+} (**Fig. 7.26**). LOD values are exceptionally low compared to the others [460-466]. A comparative study of P^5 and other reported dual Al^{3+} & Zn^{2+} sensors are

shown in **Table 2**. Study shows that the LOD of P^5 for Al^{3+} & Zn^{2+} is comparable to that reported by Alam et. al. [466]. These data indicate that P^5 is highly sensitive towards Al^{3+} and Zn^{2+} ions.

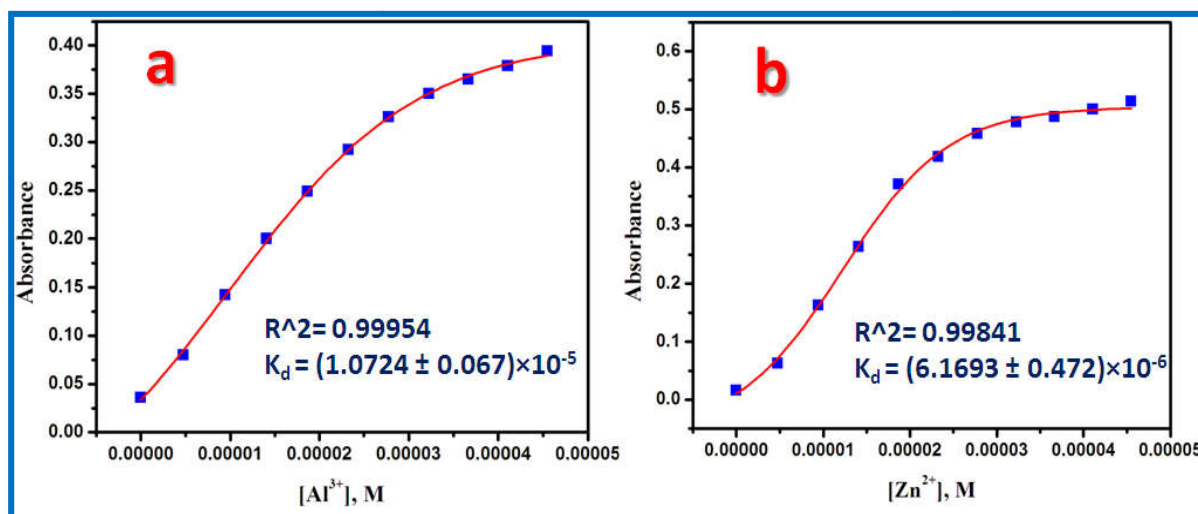


Fig. 7.24: (a) The plot of absorbance of P^5-Al^{3+} complex at 405 nm with increasing concentration of Al^{3+} (b) The plot of absorbance of P^5-Zn^{2+} complex at 425 nm with increasing concentration of Zn^{2+} .

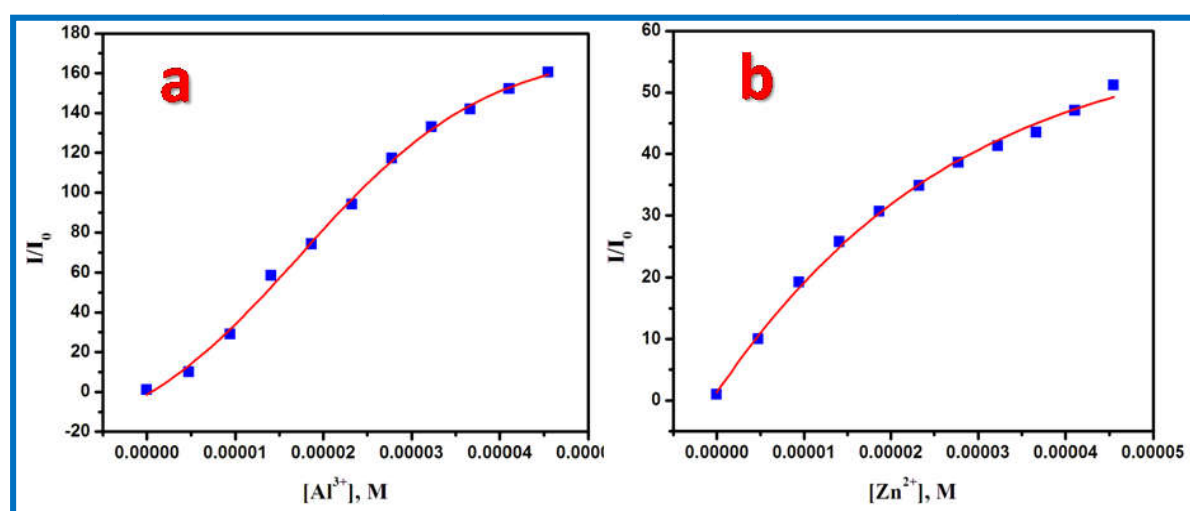


Fig. 7.25: (a) The plot of normalized emission intensity of P^5-Al^{3+} complex at 520 nm with increasing concentration of Al^{3+} (b) The plot of normalized emission intensity of P^5-Zn^{2+} complex at 520 nm with increasing concentration of Zn^{2+} .

We also demonstrate the visual detection of Al^{3+} and Zn^{2+} by sharp fluorescence changing response on TLC plate upon UV irradiation. We have prepared fluorescent test strips by dip-coating solution of P^5 in methanol on TLC plate simply followed by drying the test strips under vacuum condition. P^5 absorbed on the test strips, show no colour upon UV illumination at 365 nm. But as we irradiated 365 nm light after adding few drops (30 μ M) of Al^{3+} and Zn^{2+} each, strong yellow luminescence appears from the strip containing P^5+Al^{3+}

and green luminescence appears from P^5+Zn^{2+} containing strip (**Fig. 7.27**). This clearly signifies the solid state detection of Al^{3+} and Zn^{2+} at a very low concentration.

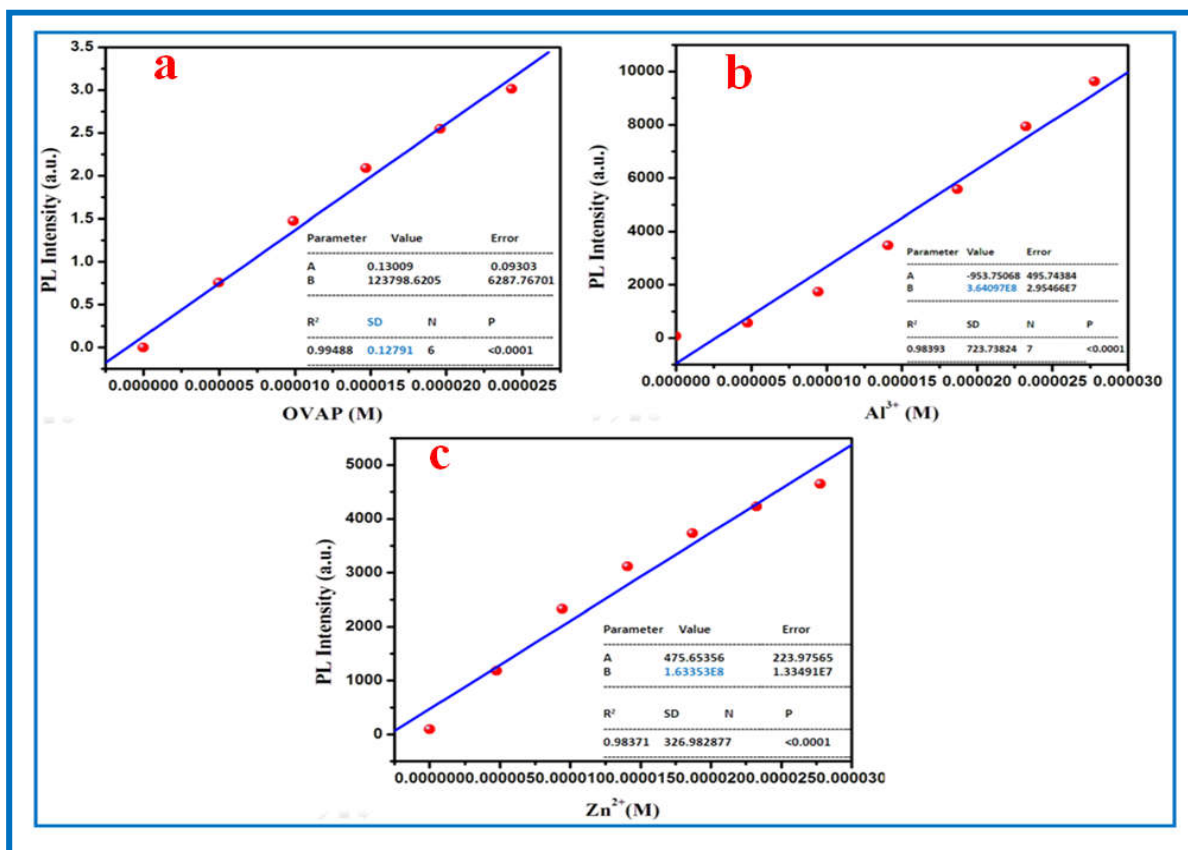


Fig. 7.26: a) Fluorescence intensity versus P^5 concentration plot for measuring standard deviation; b) Fluorescence intensity versus Al^{3+} concentration plot for measuring slope; the detection limit [LOD (Al^{3+}) = $(3 \times 0.12791)/3.64097 \times 10^8$ M = 1.05×10^{-9} M] c) Fluorescence intensity versus Zn^{2+} concentration plot for measuring slope; the detection limit [LOD (Zn^{2+}) = $(3 \times 0.12791)/1.63353 \times 10^8$ M = 2.35×10^{-9} M].



Fig. 7.27: Photographic fluorescence images of P^5 , P^5+Al^{3+} , & P^5+Zn^{2+} under UV light illumination at 365 nm.

7.3.2.7. Binding Sites and Reversibility

Stoichiometry and binding sites of P^5 with Al^{3+} & Zn^{2+} were determined by 1H NMR titration experiment (**Fig. 7.28** & **Fig. 7.29**). Upon addition of 0.5 equiv of Al^{3+} , the signal of the $-OH$ proton decreases in intensity and finally disappeared at 1.0 equiv. of Al^{3+} . A slight down field shift of 1H NMR signal of imine proton ($HC=N$) from 9.68 ppm to 9.69 ppm was observed, which strongly suggests the involvement of heteroatoms (O and N) and their chelation to form the $Al^{3+} - P^5$ complex. On the other hand, addition of 0.5 and 1.0 equiv of Zn^{2+} , the proton of the hydroxyl group at 13.039 ppm decreases in intensity and the imine proton (9.68 ppm) was shifted slightly up-field at 9.67 ppm. These results indicated that the nitrogen atom in the imine group and the oxygen atom in the hydroxyl group might coordinate to Zn^{2+} ion. No considerable changes in the position of proton signals on further addition (>1.0 equivalent) of Al^{3+} and Zn^{2+} was observed which supports the 1:1 metal to ligand ratio of the $Al^{3+} - P^5$ & $Zn^{2+} - P^5$ complex and it was further supported by the Job's plot. Again chelation site of metal ions with P^5 was supported by DFT based computational study. It has been shown that the possible location of metal ions at the imine chelation site has the lowest optimized energy structure for both $Al^{3+} - P^5$ & $Zn^{2+} - P^5$ complex (**Fig. 7.30**).

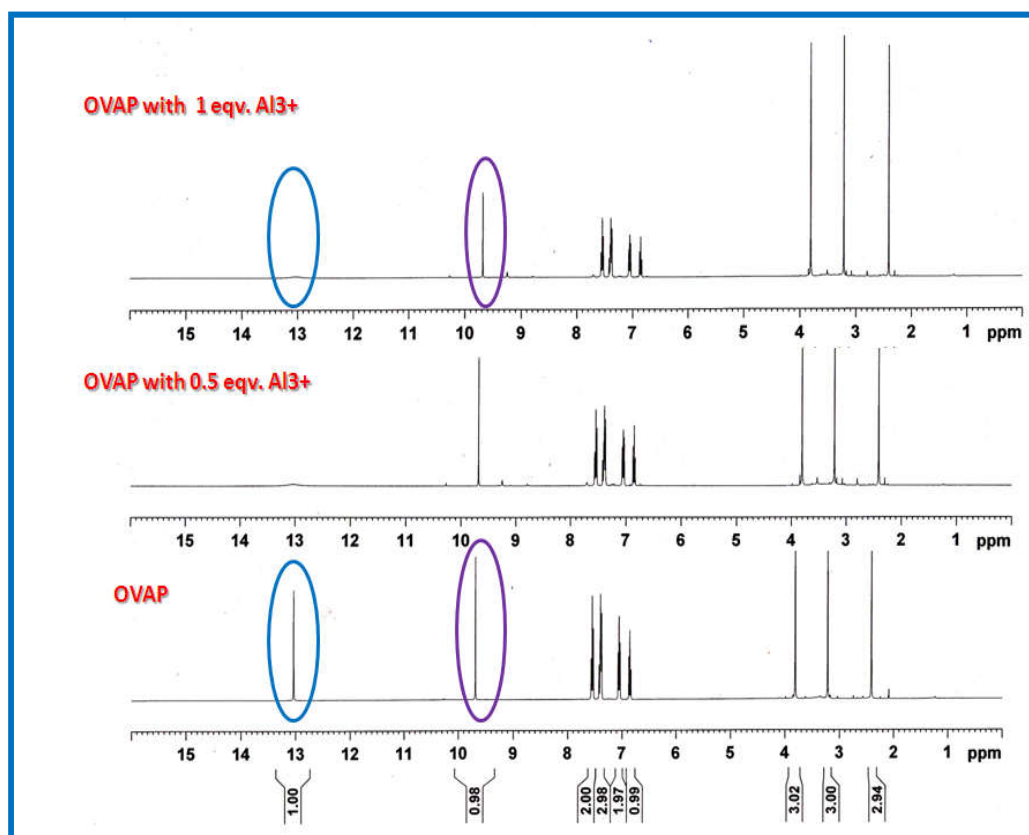


Fig. 7.28: 1H NMR (400 MHz) spectra of probe P^5 with Al^{3+} (0.0–1.0 eq.) in $DMSO-d_6$.

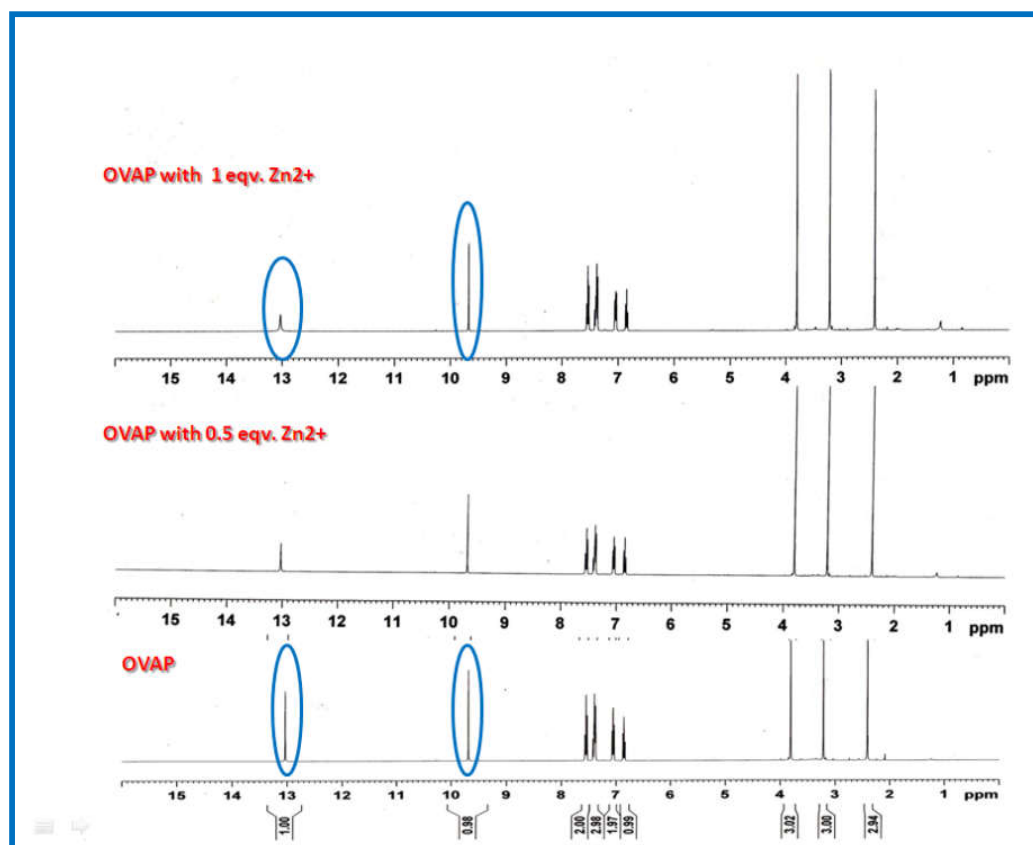


Fig. 7.29: ^1H NMR (400 MHz) spectra of probe P^5 with Zn^{2+} (0.0–1.0 eq.) in DMSO-d_6 .

Furthermore, complexation behavior was well-supported by the reversibility of Al^{3+} - P^5 and Zn^{2+} - P^5 . Reversibility is one of the most important features to convince the demand of a novel chemosensor mainly for improving practical real time applications of a probe. To examine the reversible binding of P^5 with Al^{3+} and Zn^{2+} , we used EDTA as a strong chelating ligand at identical reaction conditions (**Fig. 7.31a** & **Fig. 7.31b**). The fluorescence intensity of P^5 in the presence of Al^{3+} (at 520 nm) and Zn^{2+} (at 535 nm) decreased immediately when excess EDTA was added due to dechelation of Al^{3+} and Zn^{2+} from the corresponding complex i.e. the sensor complexes, (Al^{3+} - P^5) and (Zn^{2+} - P^5) was found to be reversible with free metal ions & P^5 .

7.3.2.8. Molecular Logic Operation

An INHIBIT logic gate is made of particular combination of the logic operation of NOT and AND functions, i.e. out-put signal is inhibited by only one type of input. To demonstrate INHIBIT logical function, one can choose two inputs Al^{3+} / Zn^{2+} (input-1) and EDTA (input-2) and the emission intensity at 520 nm/ 535 nm as the out-put. The high value of emission intensity (>31 at 520 nm (**Fig. 7.31a**) & (>17 at 535 nm (**Fig. 7.31b**)) has been assigned as 1(ON) and the low emission intensity (<17 at both 520 nm & 535 nm) has been assigned as 0 (OFF).

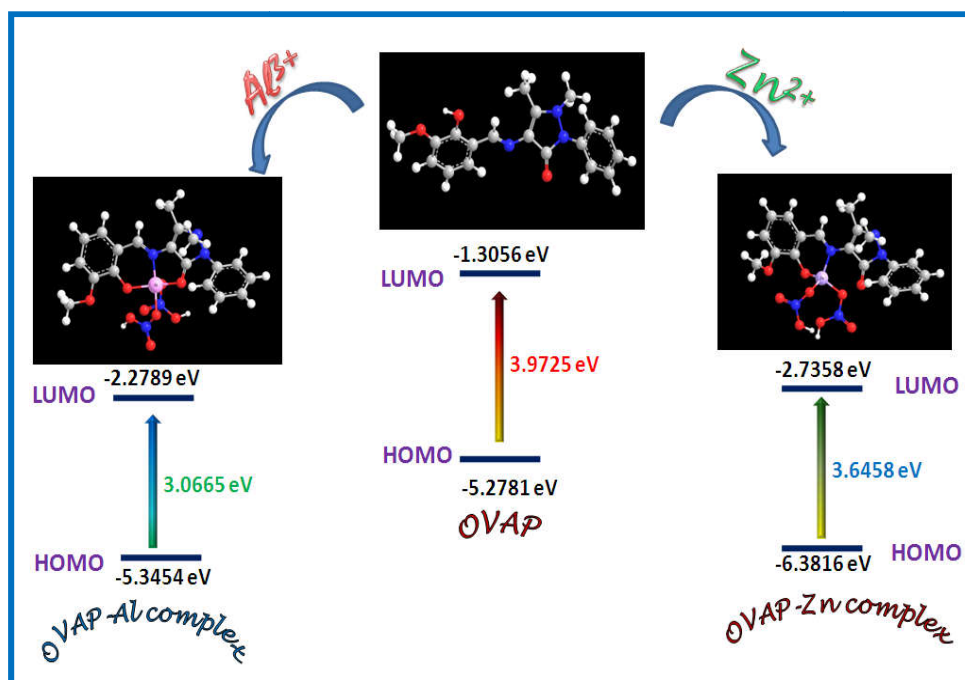


Fig. 7.30: The optimized geometry of P^5 and its corresponding Al^{3+} , Zn^{2+} complexes along with their HOMO-LUMO energy gap.

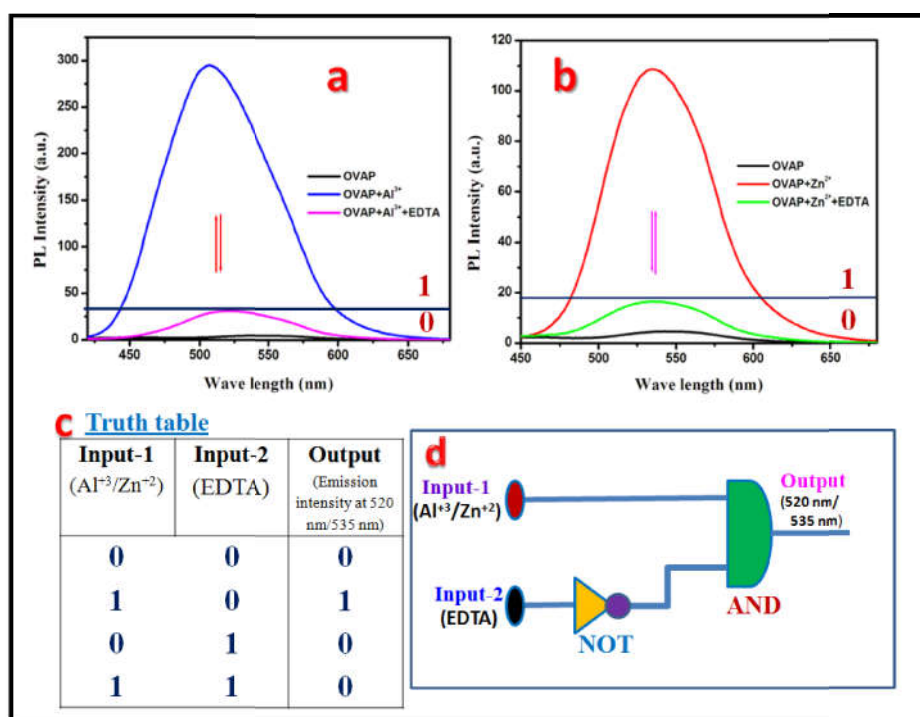
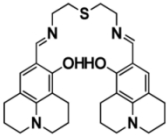
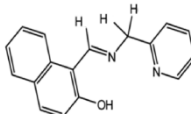
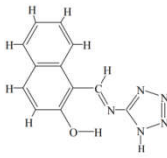
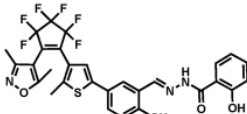
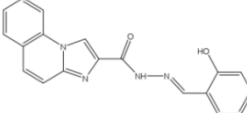
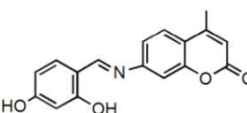
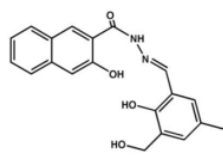
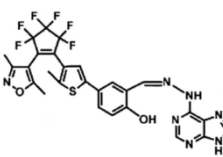
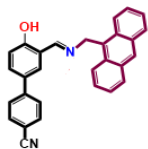
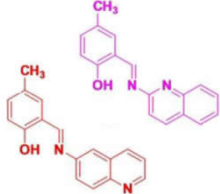
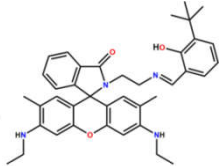
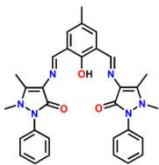
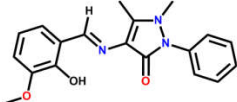


Fig. 7.31: (a) Fluorescence spectra of P^5 ($47 \mu M$) in the presence of Al^{3+} before and after the treatment with excess EDTA ($\lambda_{ex} = 360$ nm), (b) Fluorescence spectra of P^5 ($47 \mu M$) in the presence of Zn^{2+} before and after the treatment with excess EDTA ($\lambda_{ex} = 360$ nm), (c) Truth table of logic gate, (d) General representation of an INHIBIT logic gate circuit.

Table 2: Comparative Study

Sl. No.	probe	No. of steps for synthesis	Excitation/ Emission (nm)	LOD (Al ³⁺ , Zn ²⁺)	DFT study	AIEE property	Solid state study	Ref.
1		1	355/ 418 (Al ³⁺), 445 (Zn ²⁺)	1.34 μM, 1.59 μM	na	na	na	<i>RSC Adv.</i> , 2015, 5 , 11229-11239.
2		1	370/ 432 (Al ³⁺), 446 (Zn ²⁺)	0.648 μM, 1.96 μM	na	na	na	<i>RSC Adv.</i> , 2013, 3 , 25079-25085.
3		1	420/ 470 (Al ³⁺), 483 (Zn ²⁺)	5.86 μM, 1.81 μM	yes	na	na	<i>Dalton Trans.</i> , 2014, 43 , 6429-6435.
4		1	372/ 512 (Al ³⁺), 556 (Zn ²⁺)	83.10 nm, 0.33 μM	na	na	na	<i>New J. Chem.</i> , 2016, 40 , 8579- 8586.
5		5	305, 315 (Al ³⁺ , Zn ²⁺) / 450 (Al ³⁺), 489 (Zn ²⁺)	17.3 μM, 0.636 nM	yes	na	na	<i>RSC Adv.</i> , 2015, 5 , 100873- 100878.
6		4	357, 405 (Al ³⁺ , Zn ²⁺) / 427 (Al ³⁺), 496 (Zn ²⁺)	3.7 μM, 3.86 μM	na	na	na	<i>Anal. Methods</i> , 2015, 7 , 716- 722
7		2	398/ 498 (Al ³⁺), 486 (Zn ²⁺)	0.92 nM, 3.1 nM	yes	na	na	<i>RSC Adv.</i> , 2016, 6 , 1268-1278.
8		1	370/ 534 (Al ³⁺), 545 (Zn ²⁺)	6.7n M, 70.2 nM	na	na	na	<i>J. Photochem. Photobio. A, Chemistry</i> , 2019, 376 , 185-195.

9		1	365/ 390,410,435 (Al ³⁺), 477 (Zn ²⁺)	52.2 nM, 78.8 nM	yes	na	yes	<i>Sens. Actua. B Chem.</i> , 2018, 273 , 56-61.
10		1	330/ 376 (Al ³⁺), 435/550 (Zn ²⁺) 415/ 543 (Al ³⁺), 525 (Zn ²⁺)	3.79 , 136.3 nM 23.4, 53.7 nM	yes	na	na	<i>Dalton Trans.</i> , 2018, 47 , 13972-13989
11		1	500/ 550 (Al ³⁺), 370/457 (Zn ²⁺)	10.9 nM 76.9 nM	na	na	na	<i>ACS Omega</i> , 2019, 4 , 6864–6875.
12		1	390/ 480 (Al ³⁺), 508 (Zn ²⁺)	30 nM 21 nM	na	yes	yes	<i>Photochem. Photobiol. Sci.</i> , 2019, 18 , 2717-2729.
13		1	360/ 520 (Al ³⁺), 535 (Zn ²⁺)	1.05 nM, 2.35 nM	yes	yes	yes	Present work

We further defined the absence of Al³⁺/ Zn²⁺ and EDTA as ‘0’ and their presence as ‘1’. The out-put signal corresponding to four different inputs i.e. (0,0), (1,0), (0,1) & (1,1) are shown in the truth table (**Fig. 7.31c**). It is obvious from the truth table; when only input-1 is present a significant enhancement of emission intensity at 520 nm/535 nm takes place indicating the 1 (ON) state. On the other hand, when only input-2 is present the output emission intensity becomes very weak indicating OFF state. Therefore it is necessary to apply NOT gate with input-2. In presence of both inputs the emission intensity again low indicating OFF state as listed in the truth table (**Fig. 7.31c**). Thus INHIBIT function logic gate (**Fig. 7.31d**) can be constructed by the sequential application of these two input and it greatly expands the application of chemo-sensor, P⁵.

7.4. Conclusion

In summary, herein we have been able to synthesize a simple and low-cost fluorescent probe, 4-[(2-Hydroxy-3-methoxy-benzylidene)-amino]-1,5-dimethyl-2-phenyl-1,2-dihydropyrazol-3-one (**P**⁵) which is weakly emissive in solution state, but exhibits interesting aggregation-induced emission enhancement (AIEE) properties in aggregated or solid state. This emission behavior has been explained due to restriction of intramolecular rotation (RIR) and large amplitude vibrational modes of **P**⁵ in its aggregated state. Microstructures of **P**⁵ with various morphologies are synthesized using reprecipitation method. The AIEE mechanism of **P**⁵ has been explained using steady state and time resolved fluorescence spectroscopy. HOMO, LUMO electron densities of **P**⁵ reveals the intramolecular charge-transfer between antipyrine and ortho vanillin group upon photoexcitation. The present work is a judicious illustration of developing a single fluorescence-based probe for sensing dual-analytes. The ‘turn on’ luminescent property of **P**⁵ is used for dual sensing ability of trace amounts of Al³⁺ and Zn²⁺. The LODs for Al³⁺ and Zn²⁺ were determined by 3 σ methods and were found to be 1.05 nM and 2.35 nM respectively. The 1: 1 stoichiometry of the reaction between **P**⁵ and Al³⁺ and Zn²⁺ were determined by Job’s method and also supported by ¹H NMR titration. It is further demonstrated that the fluorescence ‘turn on’ emission of **P**⁵ in presence of Al³⁺/ Zn²⁺ and ‘turn off’ in presence of EDTA can be utilize to fabricate molecular INHIBIT logic gate.